Seasonal Variations of the Atmospheric Muon Rate at KM3NeT

THESIS

submitted in partial fulfillment of the
requirements for the degree of

BACHELOR OF SCIENCE
in
PHYSICS

Author :	M.E. Herschdorfer
Student ID :	S2335913
Supervisor :	Dr. D.F.E. Samtleben
Second corrector :	Dr. T.H. Oosterkamp

Leiden, The Netherlands, June 13, 2024

Seasonal Variations of the Atmospheric Muon Rate at KM3NeT

M.E. Herschdorfer

Huygens-Kamerlingh Onnes Laboratory, Leiden University
P.O. Box 9500, 2300 RA Leiden, The Netherlands

June 13, 2024

Abstract

Data from the KM3NeT detector was used to analyse the seasonal variations of the atmospheric muon rate to determine the temperature correlation coefficient α_T. The KM3NeT detector is a telescope that targets neutrino interactions, also directly offering the detection of an abundance of atmospheric muons. Studying the temperature fluctuation then can help to improve our understanding of the interactions in the atmosphere and with that also the atmospheric neutrino flux. The KM3NeT detector consists of two Cherenkov-radiation detector sites, ARCA and ORCA, that are both located in the Mediterranean sea. The data is collected with the use of light-sensitive Photo-Multiplier Tubes (PMT) integrated into Digital Optical Modules (DOM). 18 DOMs are mounted on a string that connects to the seafloor to form a Detection Unit (DU). These Detection Units form a grid to instrument a volume with the light-sensitive detectors. This setup allows for the monitoring of atmospheric muons as they traverse through the designated sites. Combining the knowledge of the depth of each DOM, the depth dependence of the frequency of the detection events, and the methods used to remove radioactive background it is possible to accurately determine the rate of atmospheric muons. To determine the atmospheric temperature at the ARCA location data is used that is collected by NASA's AIRS mission. This data consists of the Earth's surface and atmospheric temperature which is measured twice a day as infrared radiation. By comparing the muon rate and the temperature data above the

ARCA site it is possible to determine the temperature correlation coefficient α_T. The temperature correlation established from the data collected in the selected period 23/09/2022 to 1/06/2023 is $\alpha_T = 1.800 \pm 0.191$. This period was selected due to a problem establishing an accurate relative rate between May and September. The theoretically predicted value is 0.86, it is lower compared to my measured value. The study indicates a positive correlation between the seasonal variations in temperature and the atmospheric muon rate measured by the KM3NeT. However, unaccounted-for systematics may influence the result, which needs further investigation for a better understanding.

Contents

Version of June 13, 2024– Created June 13, 2024 - 15:36

Version of June 13, 2024– Created June 13, 2024 - 15:36

Chapter 1

Introduction

For as long as mankind has existed, it has looked at the stars in amazement. This is why the quest for understanding the mysteries of the universe driven by human curiosity has been one to fuel scientific advancements and explorations across civilizations. It has inspired us to keep challenging beliefs and reshape our comprehension of the phenomena around us.

A transformative event occurred in 1912 when Victor Hess discovered cosmic rays. Hess's revelation of an increased radiation at higher atmospheric altitudes contradicted the existing notion that Earth itself was the source of this radiation, revealing a new layer of complexity in our understanding of the cosmos's interaction with Earth. For this discovery he received the Nobel prize in 1936 [14]. This breakthrough triggered a radical shift in the perception of how the universe interacts with the Earth and thus opened up a whole new field of research. It, for example, led to the discovery that the cosmic radiation from astronomical sources is predominantly composed of protons and atomic nuclei.

The interaction of energetic protons with the Earth's atmosphere triggers multiple particle interactions, creating a range of secondary particles. By studying these secondary particle, Seth H. Neddermeyer and Carl D. Anderson discovered the muon and positron [20]. Muons are vital in the study of another particle that was first postulated in 1930 by Wolfgang Pauli in an open letter he sent to the group of physicists at the Gauverein meeting in Tübingen [22]. The neutrinos he postulated were a solution to the energy distribution after beta decay.

These neutrinos can tell us a lot about the universe since they have nearly no mass and are able to traverse incredible distances without interacting with other particles or electromagnetic fields. Today with sophis-

ticated particle detectors like the KM3NeT, that are designed for neutrino detection in the depths of the Mediterranean Sea, researchers have an unprecedented opportunity to study neutrinos. KM3NeT's focus is detecting muons moving upwards created by neutrino interactions but it also measures downward moving muons; this paper will look at muons moving downwards. These are known as atmospheric muons, they originate from cosmic rays interacting with the atmosphere and are one of the main sources of background in the measurement of the upwards moving muons induced by neutrinos.

The study of the seasonal variation in the muon rate started when Barret et al. first proposed and measured a seasonal dependence of interactions between cosmic rays and the atmosphere [4]. This relationship between the effective temperature of the atmosphere and the muon rate is expressed in the temperature coefficient α_T. Understanding α_T is important since it can be used to further increase accuracy in atmospheric muon simulations and neutrino analysis since currently they do not take into account seasonal variation.

Chapter 2

Theoretical Background

This chapter contains a study of the theory describing the origins of seasonal variation of the muon rate. This consists of two main concepts, firstly, the influence of temperature on the creation of atmospheric muons. Secondly, the way muons propagate through the atmosphere and the seawater and the influence thereof. This will help to understand what the governing factors are and how they influence the muon rate measured at the KM3NeT detector.

2.1 Atmospheric Muon Creation

Atmospheric muons are created in interaction between cosmic rays and the Earth's atmosphere. These cosmic rays can come from different cosmic sources and much is still unknown about their origin. However, it is generally assumed that particles below the 'ankle' at 3×10^{18} eV originate from within our galaxy and obtain their energy from supernova explosions at the site of strong collisionless shock waves [8]. It is generally assumed that the origin of cosmic rays with higher energies, up to 10^{21} eV, lies outside of our galaxy and are created by events like supernovae, active galactic nuclei, or gamma-ray bursts.

Cosmic rays encompass an array of different particles, as can be seen in figure 2.1: protons, α particles, photons, electrons, neutrinos, and atomic nuclei. When these particles collide with the Earth's atmosphere at relativistic speeds, an air shower is created. There are two types of air showers, one where the cosmic ray is a photon, electron, or positron, and where the primary particle is a proton or a nucleus. The first type results mostly in electromagnetic showers that are made up of photons and electrons. The

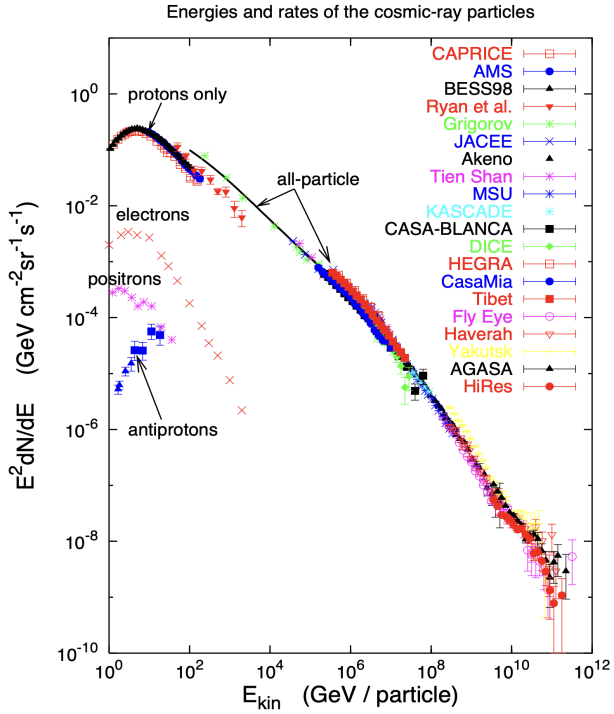

Figure 2.1: *Cosmic ray flux as a function of energy measured by many different experiments.*

[15]

second type results in a muonic component, a hadronic component, and an electromagnetic component, as can be seen in figure 2.2.

This paper will mainly focus on the muonic component which consists of muons and neutrinos. Of the three components, the muonic component penetrates the furthest and can penetrate up to several thousands of kilometers into the Earth. These muons are created by the decay of the pions and kaons of the hadronic component as shown by the following equations [9]:

$$\begin{aligned} K^+ &= \mu^+ + \nu_\mu \\ K^+ &= \pi^+ + \pi^0 \\ K^0 &= \pi^+ + \pi^- \\ \pi^+ &= \mu^+ + \nu_\mu \\ \pi^- &= \mu^- + \bar{\nu}_\mu \end{aligned} \tag{2.1}$$

Atmospheric muons are thus the product of the decay of secondary charged particles. The flux of atmospheric muons at sea level depends

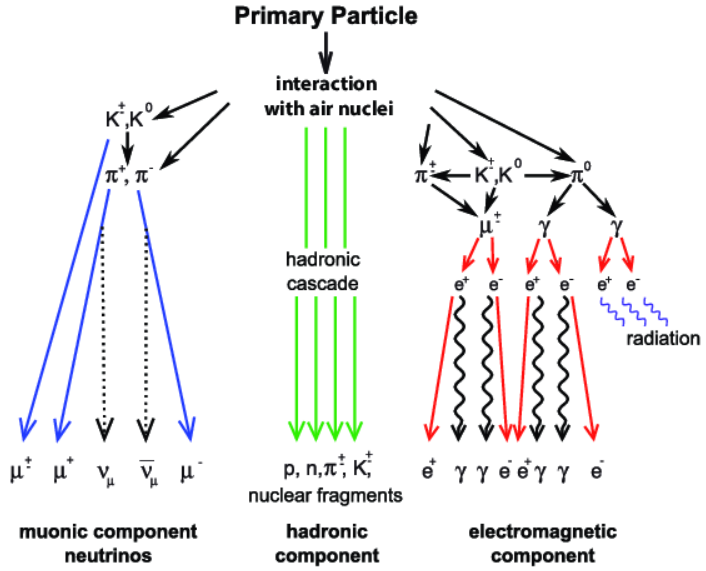

Figure 2.2: *Schematic depiction of an air shower induced by a primary particles (proton or nucleus) interaction with the Earth's atmosphere. This interaction results in secondary particles being created, mostly kaons and pions, which can directly form hadronic components, or decay in line with their decay equation, or interact with other particles in the atmosphere.*
[13]

on the frequency of interactions between the secondary particles and the probability of their decay. Which process takes place depends on the properties of the particle, like its energy and lifetime, as well as the characteristics of the air.

The lifetime of the particle is dependent on its type; neutral pions decay in $8.4 \times 10^{-}17s$ into two gamma rays, charged pions decay into muons and neutrinos, typically in 26 ns. Charged kaons decay in 12.4 ns, this means that, compared to charged pions, with the same Lorentz factor, it becomes more likely that they decay within the same time frame. This, in turn, results in a smaller decay probability for charged pions than for charged kaons [12].

Not only the type of particle play an important role, different atmospheric variables also influence whether the pions and kaons interact or decay. One of these variables is the temperature of the upper atmosphere which will be used in this thesis. Another important variable is the slant depth, this is represented by the quantity of matter the particles travel through. The slant depth is expressed by variable X:

$$X = \int_h^\infty \rho(h')\, dh' \tag{2.2}$$

Where h represents the altitude and ρ the density of the atmosphere at a specific height. The muon rate is given as

$$I(r) = I_0 e^{-r/c\tau} \tag{2.3}$$

Where r is the distance covered by the muon and τ is the life time.

2.2 Atmospheric Muon Propagation

Muons are created at a specific atmospheric depth X(h) with energy E_μ, this energy depends on the energy of the cosmic ray particle that initiated the shower. This results in a spectrum of different particles with possible energies where higher energies are less probable. Muons, just like other charged particles, lose energy as they move through the atmosphere. Generally, the energy lost correlates with the covered distance, thus shaping the muon energy spectrum at sea level. When muons reach sea level they need enough energy to traverse approximately 3 km in water before reaching the detector.

Muons, just as with pions and kaons, are unstable and have a lifetime of $\tau = 2.19 \pm 0.01 \mu s$ [17]. They are able to reach the detectors because of the speed at which they travel. The muons detected at a depth of 3500 meters below sea level need to have energies above 1833 GeV when created, corresponding with a speed of $v \approx 0.99999999667c$ [10].

When the traversed distance of a muon, traveling at 0.999c, is determined using newtonian mechanics, it results in

$$d = v\tau = 659.34m \tag{2.4}$$

Due to the relativistic speed the muon travels with, the Lorentz contraction plays a role, this results in a life time of

$$\tau = \frac{\tau_0}{\sqrt{1 - \frac{v^2}{c^2}}} = 49.2\mu s \tag{2.5}$$

This increases the distance a muon moving at 0.999c can cover in the atmosphere to

$$d \approx 14750m \tag{2.6}$$

Atmosphere

Muons, with a lifespan of $\tau = 2.2\mu s$ compared to their parent particles, can travel long distances due to Lorentz contraction and their relativistic speeds, as mentioned above. Thus, a large number of muons created in cosmic ray interactions at the atmosphere's top reach the Earth's surface, making them the most common charged particle created by cosmic rays at sea level [3]. However, not only muons and their anti particles are found at sea level, neutrinos are also abundant. Pions rarely reach the surface, as can be seen in figure 2.3, due to their much shorter lifespan of only 26 ns.

Muons with energies below 1 GeV at creation rarely reach the surface due to their Lorentz factor $\gamma = \frac{E_\mu}{m_\mu c^2} = 10$ as shown in equation 2.5. This results in a mean decay length of 6 km in vacuum, compared to the altitude of approximately 15 km where they are created. Muons with energies around 1 GeV typically decay or get absorbed in the atmosphere, as their decay length is approximately 8.7 km due to energy loss primarily from ionization [5].

Muons reaching sea level have an average energy of 4 GeV. There are variation in their energy, these variations occur because their energy pattern reflects that of the parent cosmic rays. High energy muons are created at lower altitudes due to pions traveling further before decaying, about 5.6 km. When pions have an energy of at least 115 GeV, they create lower energy pions, until their energy drops below the threshold. These lower erergy pions in term decay into lower energy muons. This causes, for high energy, a steeper spectrum for muons than pions. Muons also have a critical energy, here the energy pattern stays flat, for muons this energy is 1 GeV. When the energy of the muon is between 1 and 115 GeV, their pattern is much like that of the pions, meaning that the zenith angle has little effect. At energies greater than the critical value (115 GeV), the muon intensity is significantly lower and also decreases faster than that of the pions. Here the muon intensity is roughly 1000 times smaller than the intensity of the parent cosmic rays when these entered the atmosphere [7].

Version of June 13, 2024– Created June 13, 2024 - 15:36

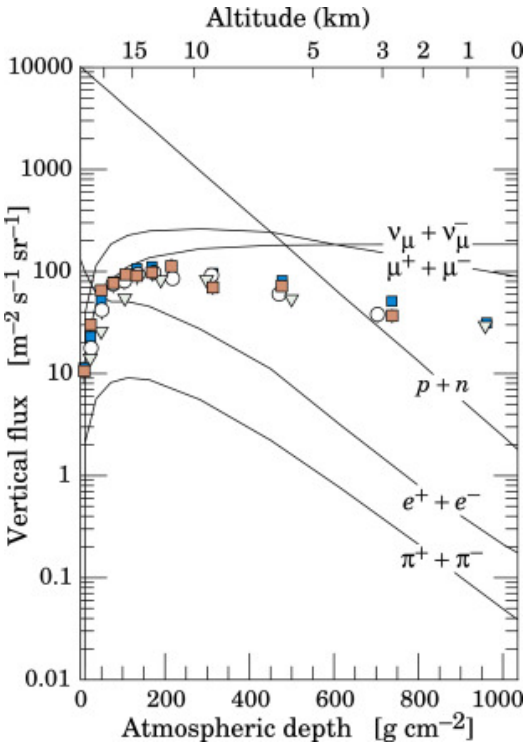

Figure 2.3: *This graph depicts the intensity of different cosmic particles, with the flux on the y-axis in $m^{-2}s^{-1}sr^{-1}$ and the altitude in km with the corresponding atmospheric depth in g/cm^2 is shown on the x-axis.*
[11]

Seawater

The muons that reach the Earth's surface still have to travel about 2 to 3 km through seawater to get to the ARCA detector. This journey causes them to lose energy, which has two causes: discrete or continuous interactions. Interactions between muons and matter results in discreet energy loss through electron-positron pair production, bremsstrahlung, and photonuclear interaction. Continuous energy loss takes place through ionization, this is the main source of energy loss for muons with energy below a few hundred GeV [6]. Because the detectors are located underwater, the high-energy muons become more important, this results in the discrete energy loss processes playing a more important role.

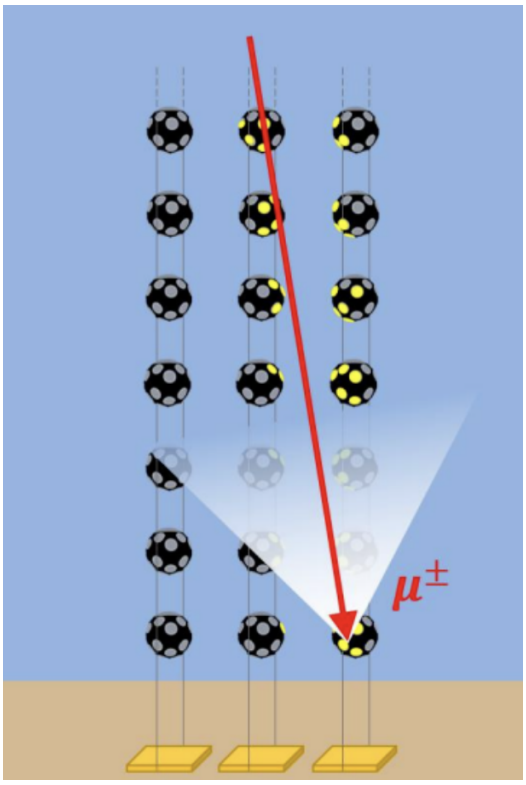

Figure 2.4: *Schematic depiction of an atmospheric muon event passing through three DU's. The shaded cone is a representation of the Cherenkov radiation emitted by the passing of the muon. Credits KM3NeT Collaboration*

The number of muons that reach the KM3NeT detector depends on the energy spectrum of atmospheric muons at sea level and how much energy the muons lose in seawater, which depends on the muon's energy

Version of June 13, 2024– Created June 13, 2024 - 15:36

and how far it has to travel. This relation is used to establish the muon rate at the ARCA detector.

To calculate the energy loss of the muons we need to determine the initial energy and quantity of the matter it has traveled through. The energy loss is linearly dependent on the initial energy of the muon and is determined as follows:

$$\frac{dE_\mu}{X} = -\alpha - \beta E_\mu \tag{2.7}$$

Where X represents the thickness in grams per square centimeter, α is the continuous loss in due to ionization, and $\beta = \beta_{brems} + \beta_{pair} + \beta_{photop}$ is the sum of the fractional energy loss from the radiative processes. This is complicated because α and β are energy dependent. The critical energy where ionization becomes more important than radiative loss is $\epsilon = \frac{\alpha}{\beta}$.

Solving equation 2.7 gives the muon average energy dependent on depth

$$\langle E(d) \rangle = (E_0 + \epsilon)e^{-\beta d} - \epsilon \tag{2.8}$$

E_0 is the initial energy at d = 0 and ϵ is the critical energy mentioned above, from this equation it is possible to derive an expression for the minimum energy needed to reach a certain depth.

$$E_{0,min} = \epsilon(e^{\beta d} - 1) \tag{2.9}$$

Muons reaching depth d have no energy left to produce the Cherenkov radiation* that is needed for detection. The energy needed to produce Cherenkov radiation can be determined using the following equation:

$$E_c = \frac{m_\mu c^2}{\sqrt{n^2 - 1}} \tag{2.10}$$

Here m is the mass of the muon, c is the speed of light, and n is the refractive index of the medium which for seawater is approximately 1.33. Solving this equation results in $E_c \approx 130 MeV$, this is relatively small compared to the energy needed to reach the depth of the detectors.

Equation 2.9 can also be used to find the depth a muon with a certain energy will reach.

$$d = \frac{1}{\beta} \ln\left(1 + \frac{E_0}{\epsilon}\right) \tag{2.11}$$

*What Cherenkov radiation is and how it is induced is explained in chapter 3.2

Because the detectors are set up at varying depths, the deeper the detector the fewer muons it will measure and thus have the lowest rate. To compensate for this the following approximation is used

$$R(d) = ae^{-b(d-2740)} \tag{2.12}$$

Here R is the depth dependent rate, a is the rate at 2740 meters depth[†] and b is the exponential slope which is a fitting parameter. How this is used to determine the final rate is explained in the methodology chapter.

2.3 Atmospheric Dependence

As mentioned before, the number of muons created depends on the energy of the parent particle and the density of the upper atmosphere. Whether muons are created depends on the balance between the interaction of the particle with the atmosphere and the decay probability. So, altering the temperature of the upper atmosphere by ΔT affects the total muon intensity by ΔI_μ. The decay and interaction paths are separated by the critical energy (ϵ_i) as shown below.

$$\epsilon_i = \frac{M_i c^2 RT}{c\tau_i Mg} = \epsilon_i(T_0)\frac{T}{T_0} \tag{2.13}$$

Here T_0 is the temperature at sea level and this equation is equivalent to the relation mentioned above $\epsilon = \frac{\alpha}{\beta}$. From this relation it is clear that there is an inverse relationship between lifetime and temperature, meaning that more mesons decay, resulting in higher muon creation, as temperature increases.

How this affects the measured muon rate at ground level depends on the energy of the muons. For high-energy muons detected at ARCA the variation in temperature has less influence. This is due to the higher speeds they travel with causing a shorter time frame in which they can decay.

However this is different for lower-energy muons; because the atmosphere expands due to higher temperature, the distance to be covered by muons also increases. Consequently, fewer lower-energy muons reach the detector. Combining these effects the temperature has on muons reaching the detector results in a positive correlation between the intensity and the temperature as shown below.

[†]This is the depth of the top of the detector

$$\frac{\Delta I_\mu}{I_\mu^0} = \alpha_T \frac{\Delta T}{T} \tag{2.14}$$

Here α_T is the temperature coefficient. This equation is then used to derive the final equation used to determine α_T:

$$\frac{\Delta R_\mu}{\langle R_\mu \rangle} = \alpha_T \frac{\Delta T}{\langle T \rangle} \tag{2.15}$$

How the rate and temperature are measured is elaborated in the methodology chapter.

2.4 Previous research

Due to the existence of multiple detection sites for neutrinos, that share similar muon sensitivity, there are different studies into the seasonal variation of muons. The study that is considered to be the first to look for a correlation between the temperature and the muon rate is Barret et al. [4]. Because these detection sites differ on many levels, for instance location, surrounding material, or depth, the correlation is different for each site. The effect this has on α_T can be seen in figure 2.5.

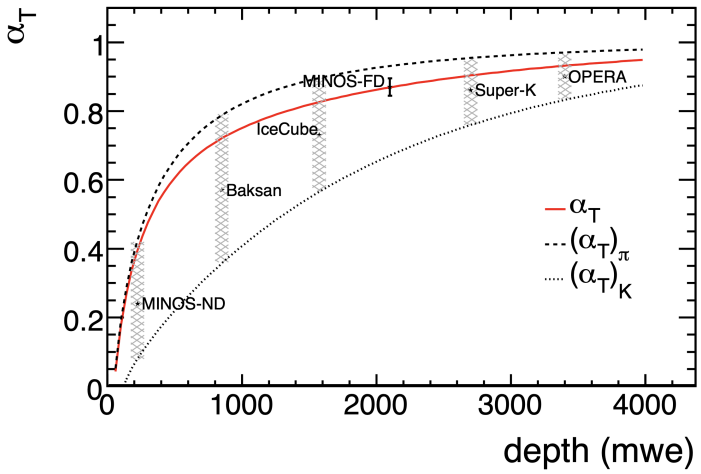

Figure 2.5: *The theoretical $\alpha_T(X)$ for for muons for different detection sites is depicted by the red line. The dashed line is a representation of $(\alpha_T(X))_\pi$ for pions and $(\alpha_T(X))_K$ is represented by the dotted line for kaons. All for slant depths up to 4000 meter water equivalent (mwe).*

[10]

Looking at the depth the ARCA site is located, the expected $\alpha_T = 0.86$; this is, however, an approximation.

Studies have also been conducted into the correlation at the KM3NeT ORCA site, the results from this research can be seen in figure 2.6.

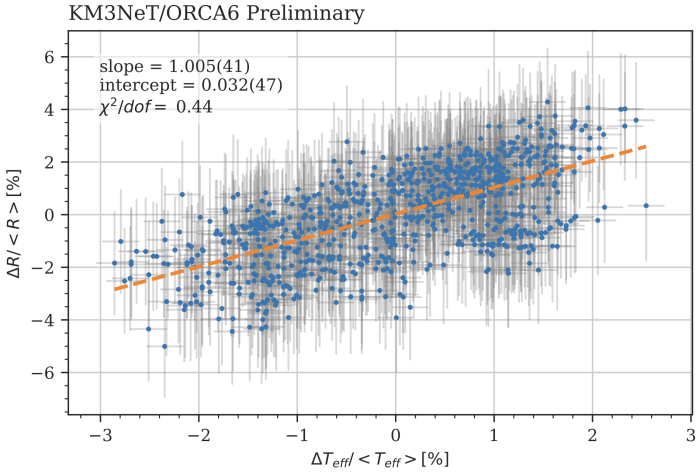

Figure 2.6: *Correlation between the atmospheric muon rate and the effective temperature. Here* $\alpha_T = 1.005 \pm 0.041$

[19]

Furthermore, this has also been concluded by a master student last year for the ARCA site, who showed the following results.

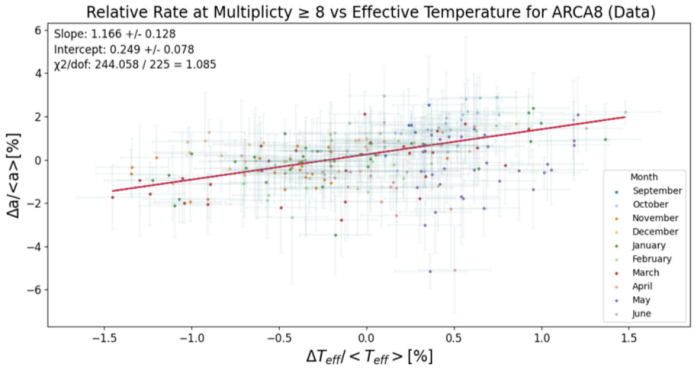

Figure 2.7: *Correlation between the atmospheric muon rate and the effective temperature of multiplicity equal or higher than 8. The data used in this plot was only obtained by ARCA 8. She found a value for* $\alpha_T = 1.166 \pm 0.128$

[24]

The research conducted at the MINOS far detection site resulted in $\alpha_T = 0.873 \pm 0.009$. This site is located in Northern Minnesota at a depth of 716 meter, was assumed to be equal to a water depth of 2080 meter.

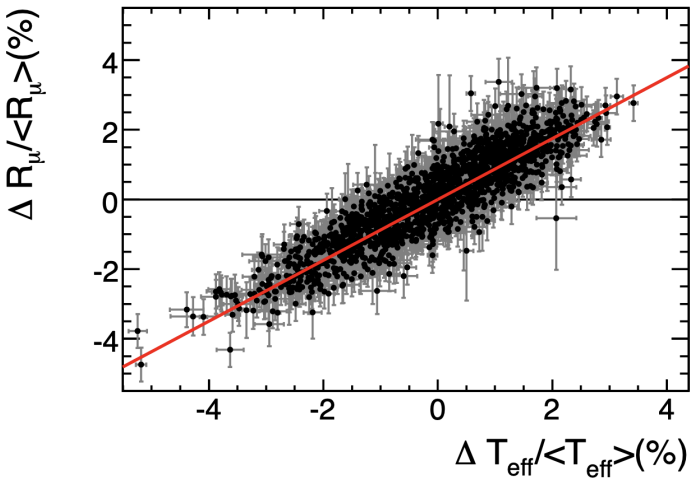

Figure 2.8: *Correlation between the atmospheric muon rate and the effective temperature, the line is fitted to go through the origin, this sets it apart from the other studies.*

[1]

Chapter 3

Detector

The KM3NeT neutrino telescope consists of two sites, ORCA and ARCA, both with a different focus. Even though both sites have been active for quite some time they are still under construction and should be completed in 2028.

The ARCA (Astroparticle Research with Cosmics in the Abyss) site is located 80 km off the coast of Capo Passero in Italy at a maximum depth of 3450 meters. The focus of this site lies in discovering and learning more about the sources of the astrophysical neutrinos. This results in studying the energy spectrum and flavour composition of the neutrinos, thus the site is set up to measure neutrinos within the energy range of 1 TeV to 10 PeV. This required a bigger distance between the detectors than for ORCA.

The ORCA (Oscillation Research with Cosmics in the Abyss) site is located 40 km of the coast off Toulon in France at a maximum depth of 2450 meters. This sites focuses on measuring the oscillation properties of the neutrinos, this allows them to determine the neutrino mass ordering. They measure these properties by measuring the atmospheric neutrinos which are most commonly found within the energy range of 1 - 100 GeV. Because they focus on this energy range, the telescope is situated at a lesser depth and the detectors are placed closer together than with ARCA.

3.1 Construction

The KM3NeT detectors consist of multiple detection units, these are long strings connecting 18 Digital Optical Modules (DOM). Each of these DOM's consists of 31 Photo-Multiplier Tubes (PMTs), 19 of these PMTs are located at the bottom half of the DOM and the remaining 12 on the top half as can

be seen in figure 3.1.

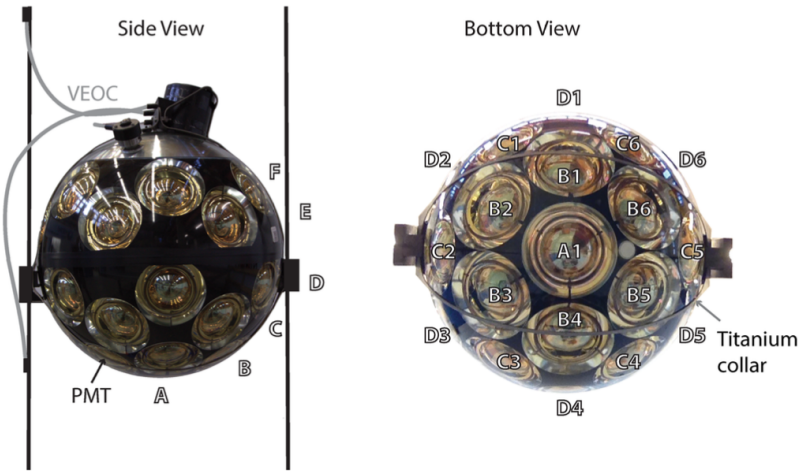

Figure 3.1: *A side view (left) and bottom view (right) of a DOM. Each ring of PMTs is labeled with a letter and within each ring every PMT is numbered. The DOMs are made from pressure resistant glass and have a diameter of 43 cm.* [18]

The PMTs are distributed in this way because the way the neutrinos are detected, these are neutrinos that have traveled through the Earth, interact, and create a muon. Because these muons move upwards, it is beneficial to place the majority of the PMT's on the bottom. To provide a better understanding of what the detector looks like and how neutrinos are measured, a schematic depiction of such an detection event can be seen in figure 3.2. The PMTs measure the muons by detecting light they create when moving through the water, called Cherenkov radiation, this is further explained in the section below. To further improve the signal, the PMTs are fitted with a reflector ring and are filled with transparent optical gel, this gel ensures that the PMTs are optically coupled to the inside of the sphere. This results in approximately $\frac{1}{3}$ of the photons that hit a DOM being registered.

As mentioned above, each Detection Unit (DU) consists of 18 DOMs that are connected with an electro-optical cables. These cables are essential since they transfer all the collected data to shore. To keep the detection units in place, they are connected to the seabed using a weight and kept aligned via a buoy at the top.

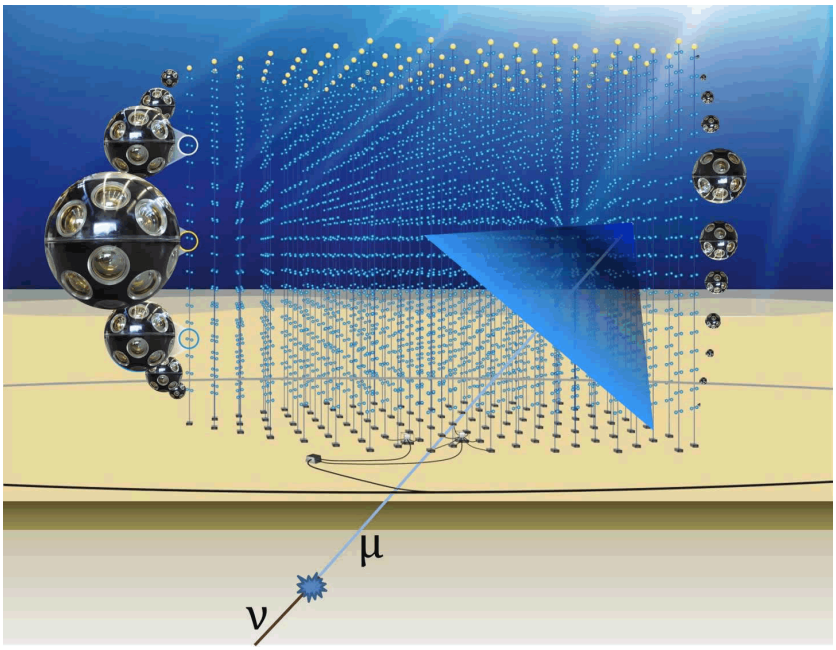

Figure 3.2: *This figure depicts an upwards moving neutrino interacting and creating a muon. Because it is very hard to distinguish muons created in such an event and the downward moving atmospheric muons the widely used method consists of looking at the direction the muon is moving. This can be distinguished by the sequence the PMTs are triggered. Credits KM3NeT*

Because of the different scientific goals of the ORCA and ARCA detectors, their spacial orientations are different. To improve lower energy range neutrino detection, the DUs are placed 20 meters apart with a DOM every 9 meters. To improve higher energy neutrino detection, in the ARCA site the DUs are 90 meters apart with a DOM every 36 meters.

3.2 Cherenkov Radiation

As mentioned above the PMTs are able to detect muons and indirectly also neutrinos due to muon's Cherenkov radiation. They detect neutrinos using this method because of their elusive nature of neutrinos which makes direct detection impossible. When neutrinos interact, they create secondary particles, which contain information about the neutrino's energy, direction, and flavour. There are three different neutrino flavours, tau neutrino, muon neutrino, and electron neutrino. All three produce correlating leptons [21]. Because the pattern of the light the Cherenkov radiation produces differs for every lepton they can be distinguished.

Cherenkov radiation is produced when a charged particle moves through a medium faster than light moves through that medium. When these charged particles move through a medium they create a wavefront and emit Cherenkov radiation, compare this to the sonic boom created by objects moving faster than the speed of sound. Since the energy range of muons is known, it is clear they can have the capability to exceed the speed necessary to produce this effect [23]. Since the KM3NeT detectors are located in sea water with a refractive index of n = 1.33, this results in:

$$v_{CR} > \frac{c}{n} \approx 0.75 \tag{3.1}$$

A schematic depiction of such a wavefront is shown figure 3.3, the angle at which the wavefront is emitted is called the Cherenkov angle. This angle is dependent on the particle's speed relative to the speed of light $\beta = \frac{c}{v} \approx 1$ and can be determined as follows:

$$cos(\theta_C) = \frac{1}{\beta n} \tag{3.2}$$

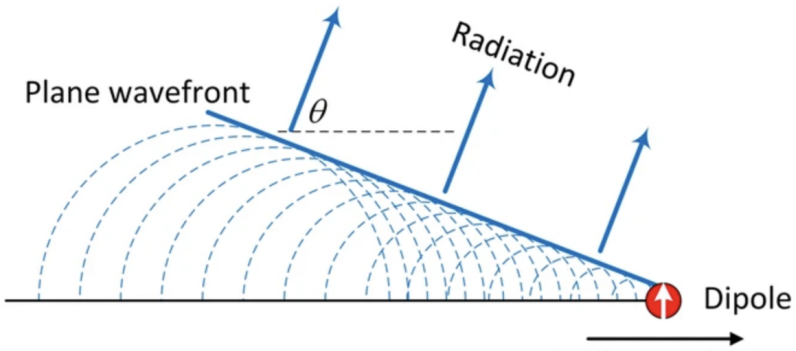

Figure 3.3: *Schematic depiction of a particle creating a Cherenkov Radiation wavefront.*

[16]

The combination of equation 3.1 and 3.2 results in an angle of approximately 41°. A well-known example of this kind of radiation is visible inside the heavy water surrounding nuclear reactors, which emit a blue glow.

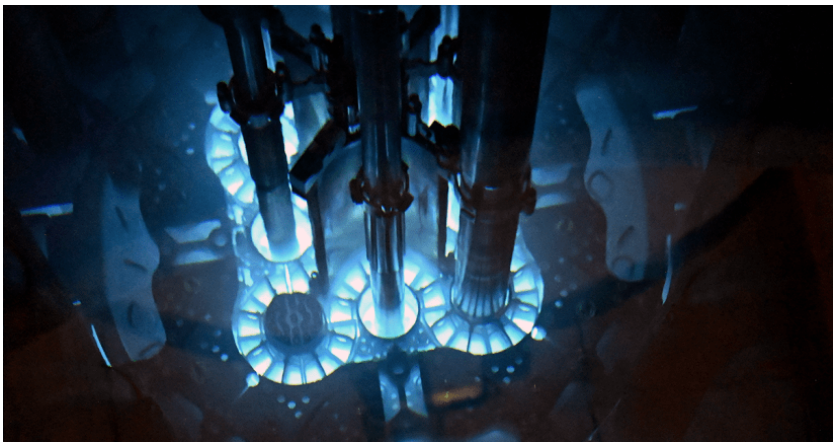

Figure 3.4: *Cherenkov Radiation captured inside the Advanced Test Reactor at Idaho National Laboratory. Credits Office of Nuclear Energy*

3.3 Data Acquisition

When a charged particle, with energy above the threshold moves through the detectors it creates photons which are detected by the PMTs. When the PMTs detect these photons they register the duration the photons are measured and the time of the event. This information is sent to the data collection site on shore as an L_0 hit. When an event triggers multiple PMTs within the threshold of 25 ns, the event is registered as a L_1 hit. Most of these hits are caused by radioactive decay. An event can trigger a varying number of PMTs depending on the energy of the charged particle, the number of PMTs triggered is called the multiplicity. All L_1 hits with a multiplicity ≥ 4 are stored. The multiplicity is elaborated further in chapter 4.1.1. The detectors are not continuously measuring but are turned on periodically, every measuring period is called a run and multiple runs can take place per day. The duration or a run is typically 3 hours, but it can differ per DOM, the runtime for every DOM per run is collected and taken into account in the analysis. The runs analysed span from 23/09/2022 to 11/09/23.

3.4 Background Noise

Apart from muons there are multiple other sources that also produce Cherenkov radiation or detection events. Most of the events that are recorded are from ^{40}K decay and bioluminescence which both will be explained further

below. Another big source of noise to the detection of neutrinos are the atmospheric muons, which is why understanding their behaviour better is important and the goal of this thesis.

3.4.1 ^{40}K Decay

Potassium-40 is a radioactive isotope that occurs naturally in sea water and thus can abundantly be found in the Mediterranean. ^{40}K can decay in two different ways, of which β decay accounts for 89.3%. For this type of decay, the electrons that are ejected can have energies above the threshold needed to produce Cherenkov radiation. However, these electrons generally have a lower energy than muons which causes the events to be of lower multiplicity. This is why we implement a multiplicity selection on the data which is further explained in the methodology chapter.

3.4.2 Bioluminescence

Bioluminescence originates from organisms that live close to the detection sites and emit light. This bioluminescent light can cause large fluctuations in the received signal over time. However it can be recognised by a specific DOM receiving an increased amount of light over a period of multiple seconds. To counter the effect of the bioluminescence they have employed multiple techniques. The first technique they use is as soon as the count rate exceeds 20 kHz in PMTs, they close the channel and remove the data. Further, once a count has been detected above the threshold, a timeslice of 100ms is blocked from detection. This system is called the High Rate Veto (HRV).

Chapter 4

Methodology

This chapter delves into the data acquisition and data analysis utilised in the process that leads to finding a value for α_T. This process consists of determining the muon rate, determining the effective temperature, and the comparison between these two that leads to α_T.

4.1 Rate Determination

The start of this process is determining what the actual muon rate is at the KM3NeT ARCA detector. To determine this, multiple methods are used to make it more accurate, starting with the multiplicity to separate the background signals from that of the muons. Thereafter, it is explained how the depth dependence and the efficiencies of the PMT's influences this rate. The rate is determined for each DOM, this is combined to determine a collective muon rate for the ARCA detector.

Quality Cuts

Quality cuts make sure the results derived from the raw data are reliable, this is essential since the raw data is not extensively checked for quality. Runs with issues such as DOMs with short runtimes, or disturbances at specific DOMs are still present in the data. These cuts ensure that above mentioned issues do not lead to large fitting errors and extreme outliers in the χ^2/dof distribution of the fits.

Version of June 13, 2024– Created June 13, 2024 - 15:36

4.1.1 Multiplicity

To determine the atmospheric muon rate using the KM3NeT detector, it is important to understand what multiplicity is and the role it plays in coincidence measurements. Most photons that are detected by the PMTs within the DOMs do not come from muons emitting Cherenkov radiation, the measured signal primarily consists of photons emitted by the decay of ^{40}K present in sea salt and bioluminescence, as explained in the detector chapter.

To be able to distinguish the atmospheric muons and the background sources multiplicity is deployed, this refers to the number of PMTs registering a detection event, this is called an L1 hit. High-energy particles like atmospheric muons can light up numerous PMTs within a DOM, resulting in high multiplicities. Low-energy processes, such as ^{40}K decay, light up only a limited number of PMTs.

Previous studies of KM3NeT showed that up to multiplicity 6 the signal is dominated by the decay of ^{40}K as can be seen in figure 4.1. This also led to the observation that atmospheric muons become dominant around multiplicity 6, and full dominance of atmospheric muons in the signal is assumed at a multiplicity of 8.

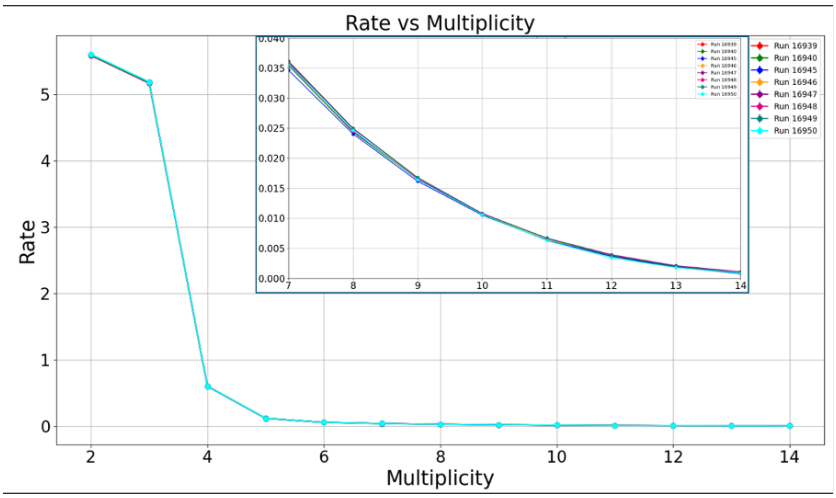

Figure 4.1: *The rate from 8 different runs as function of the multiplicity, it shows the transition from ^{40}K decay dominance into atmospheric muons. Inset is zoomed in on multiplicity 7 to 14.*

To make sure the background signal is filtered out effectively, the first approach used is selecting coincidence counts with multiplicity equal or greater than 8. This will mitigate the influence of the ^{40}K decay to the

signal. This leaves the summation of all hits with a multiplicity of 8 or greater in each run, after which this is corrected for the length of the run and DOM efficiency, it then provides a solid measure for the atmospheric muon rate.

The analysis of the signal with multiplicity smaller or equal to 4 will show the effect of the ^{40}K decay. This step is important because it acts as a verification of the stability of the method because for ^{40}K decay there should be no seasonal change or depth dependence in the signal. Both these steps involve the extraction of atmospheric muon hits from the root files. The effect multiplicity has on the rate and the exponential fit parameter that represents the slope can be seen in figure 4.2.

To understand the multiplicity better, an analysis of the coincidences at each DOM is used, this allows for a more precise determination of the atmospheric muon rate.

4.1.2 Depth Dependence

Determining the muon rate at the ARCA detector involves an elaborate consideration of depth dependence to improve precision and reduce susceptibility to systematic fluctuations unrelated to seasonal changes. Rather than measuring the rate at each DOM during a full year, the DOMs in a run are used to calculate the muon rate, using the well-known depth dependence of atmospheric muons.

As explained in the theory section, high-energy muons reaching the DOMS of the ARCA detector, positioned at varying depths, from 2740 to 3400 meters, lose energy due to discrete radiative processes. This results in an expected atmospheric muon rate, described by the equation $R(d) = ae^{-b(d-2740)}$.

The depth-dependence model provides a strong foundation for rate determination, as individual DOM fluctuations become less significant when data from all DUs combined is used to determine the behavior of the fit. While using one DU could suffice, adding more reduces uncertainty in the rate measurement.

Figure 4.2 shows an example of the depth dependence, on the basis of the measured rate, corrected for the efficiency of each DOM for a run 16947*. Each colour represent a different string and the red line is a the best fit based expected relationship between the rate and the depth. This shows the behaviour of the DUs, and if a DU behaves significantly differently

*A run typically lasts 3 hours but it can fluctuate per DOM. This can be seen in figure 5.3

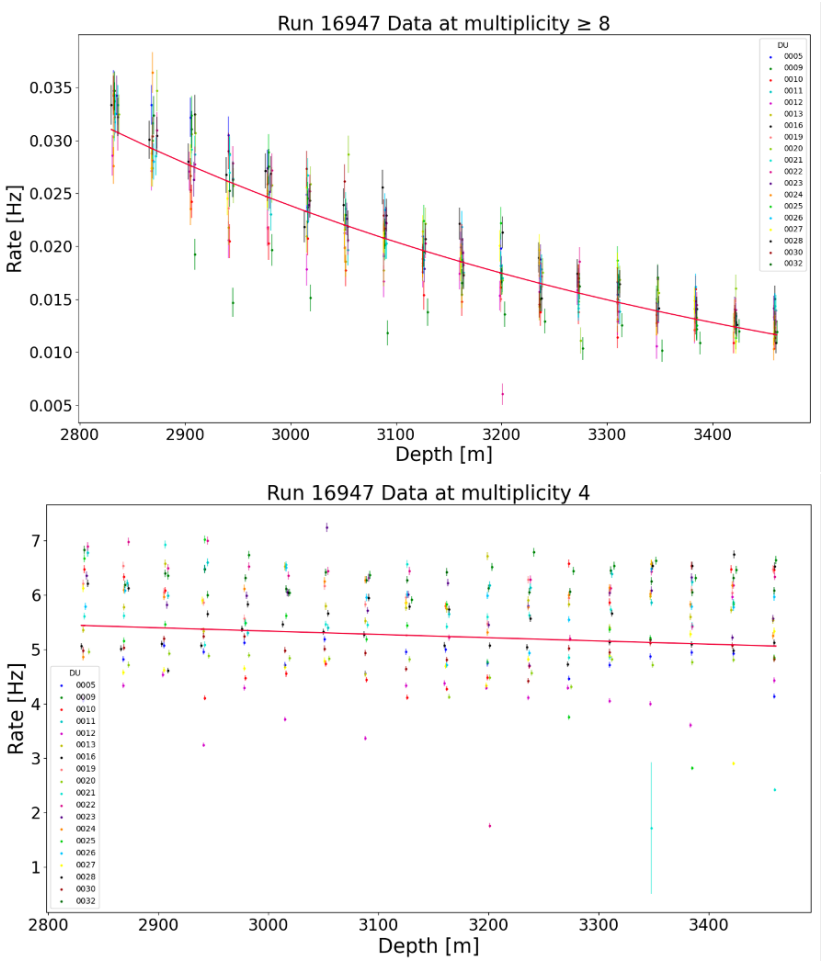

Figure 4.2: *Every data point represents the relation between the depth and the measured rate at that DOM. Each colour represents a different DU and the red line is the fitted depth dependence of the rate. As expected, there is no depth dependence at multiplicity 4.*

from other DUs, such as 0009. This can then be used to justify the exclusion of certain DUs from further analysis to better the determination of the rate.

To obtain the fit parameters a and b, similar plots are generated for all runs, where a represents the atmospheric muon rate at 2740m below sea level, b represents the slope fitted to the data. This cannot only be used for determining the rate but also to asses the accuracy of the results by comparing b to the predictions made based on the theory. For multiplicity 4, which is dominated by the ^{40}K decay, it is expected to be a constant slope since the difference in salinity and the ^{40}K concentration between 2700 and 3400 meters does not vary much.

4.1.3 Rate Correction

In order to obtain a precise measurement of the atmospheric muon rate, we need to perform a few corrections on the raw coincidence count. The sum of the number of hits higher or equal to multiplicity 8 still needs to be corrected to account for the PMT efficiencies and the length of each run before the comparable quantity is acquired.

Efficiency

Efficiency plays an important role in determining the atmospheric muon rate detected by the KM3NeT detector. As explained in the detector chapter, the PMT photon detection efficiency encompasses the PMT quantum efficiency, collection efficiency, angular acceptance of the PMT, and absorption of the gel and glass. Furthermore, a systematic error of 5% is applied. To calculate the efficiency correction for each PMT, a systematic approach is used, and the efficiency is determined for each PMT within every DOM for a set of multiple combined runs because there is only limited statistical data in individual runs. To determine the efficiency of the PMTs the homogeneous signal from ^{40}K decay within a DOM is used.

Since the rate is available for each DOM rather than each PMT, the PMT efficiencies must be used to compute an overall DOM efficiency. A weighted average is calculated for this purpose, taking into account the weight associated with each PMT and their corresponding efficiency. The weights used by Lara Skrabal were also used in this study and were determined using the probability density function, this shows the contribution of each PMT to the coincidence count based on the multiplicity variation[24]. This weighted approach is essential because the detected signal is direction dependent. Atmospheric muons, being predominantly

detected by the top PMTs, need careful consideration of the contribution of each PMT in the efficiency calculation.

To ensure the depth dependence method works, the measured rate is corrected using the exponential fit parameters. This results in the expected linear relationship between the rate and the efficiency as can be seen in figure 4.3. This shows that the approach using the depth dependence to determine the atmospheric muon rate is effective.

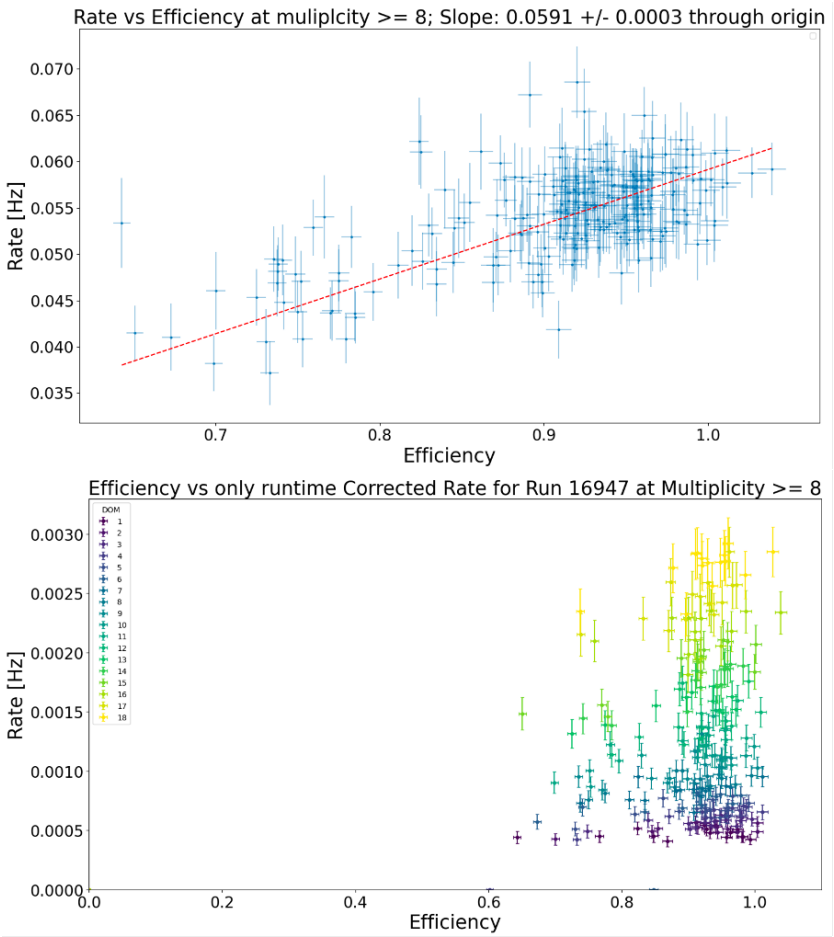

Figure 4.3: *Top: The linear relation between the rate and the efficiency. Bottom: Without depth correction it can be seen that the lower numbered DOMs, which are located at the greatest depths, have a much lower rate, as expected.*

This meticulous efficiency determination is very important in ensuring that the measured signal is proportional to the atmospheric muon rate, providing a foundation for the following analysis and interpretation of the KM3NeT detector data.

Runtime

To be able to ensure that the muon rate across different DOMs is accurate and comparable, a correction of the runtime is necessary. This is to account for the variation in the time each DOM was operable during each run. Without this correction, it would be impossible to obtain the rate in Hertz, which allows for the comparisons and analyses that are required.

In this process, the efficiency-corrected coincidence count for each DOM is divided by its specific overall runtime. The runtime is provided in seconds, is highly accurate, and ranges between 3 to 6 hours. The runtime is provided in such accuracy that any error in the measurements is negligible, accounting for less than 0.01% for a runtime of 3 hours.

The error in the final corrected rate originates from two main components: statistical Poisson error and the 5% systematic error in the efficiency of the PMTs. The PMT efficiency is used through the weighted averages that are used for the DOM efficiency correction. This contributes to the overall error in the measured muon rate. The corrected rates are then plotted against the depths that correspond to the DOMs, as shown in figure 4.2.

4.1.4 Relative Rate and Daily Average

Since normally there are multiple runs in a day, the fit parameters and errors need to be averaged over all runs of that day to be related to the daily average temperature.

Relative Rate

In the final analysis, it is not the rate but the relative rate that is compared to the effective temperature, as defined by equation 2.15. The relative rate is the rate compared to the mean of the considered time period.

Daily Average

After applying the quality cuts, to determine the relative rate and the daily average, the daily mean of the fit parameters is calculated. The data points show a spread inconsistent with statistical scatter. So we need to account for further systematics and the spread is exploited as measure of the systematic error. This then needs to be accounted for in the estimated error of the mean, this error is further increased by an intrinsic error from

a limited amount of data points available to calculate the daily average.

4.2 Effective Temperature Determination

The relative atmospheric muon rate is compared to the effective atmospheric temperature; to obtain the effective temperature, the temperature data is analysed as discussed in the following section.

Obtaining the Data

The atmospheric temperature data that is used is collected by NASA's Atmospheric Infrared Sounder (AIRS) mission. The data is collected by a grating spectrometer that measures the infrared energy emitted by the Earth's surface twice a day.

The data collected by this mission includes date time records, pressure levels, temperature measurements, standard deviations, and latitude-longitude coordinates for each measurement point. The average temperature is obtained using a grid centered on the location of ARCA ($36°16'N, 16°06'E$), which is extended by one degree in latitude and longitude.

Calculating the Effective Temperature

The dataset consists of temperature measurements and their corresponding standard deviations for 24 pressure levels ranging from 1 to 10000 hPa, which is sampled twice daily. The measurement times from the AIRS mission do not align with the runs from ARCA, because of this, the daily averages of the temperature values and the fit parameters were calculated, with their respective errors.

The calculation of the effective temperature involves assigning weights to specified effective areas of the detectors, these were established by J. Mulder [19] for KM3NET. Since the pressure levels in space are non-uniformly distributed, the weighted average would not yield accurate results. This problem is solved by using Simpson integration, leveraging Python's numerical integration capabilities. This allows for integration over discrete samples along the pressure axis.

4.3 Temperature Coefficient α_T

The temperature coefficient α_T can be determined, after the effective temperature and its error have been established, using a similar method to that of the relative atmospheric muon rate. This can be done according to equation 2.15 where the temperature coefficient is derived from the slope of a linear regression fit. To accurately do this, it is important to account for the errors in the x and y directions. This is done using orthogonal distance regression because standard linear regression models only account for the error in the x direction. To test the quality of the fit, the chi-square value is used to determine how well it represents the data points.

Chapter 5

Rate Analysis

To determine the rate multiple steps need to be taken. First, determine the coincidence count, this can then further be analysed and corrected for multiplicity, coincidence count, runtime, and efficiency. This chapter will show the effect of every correction, ending with the relative rate per date. This will be used in the final analysis combined with the effective temperature to determine α_T.

5.1 Multiplicity

A selection of the data is made based on multiplicity, why and how is explained in the methodology chapter. Figure 5.1 gives a visual representation of the effect of the multiplicity on the rate and the exponential slope. From the top graph in figure 5.1 it is clearly visible that the rate decreases as the multiplicity increases, this correlation is strongest for the lower multiplicities, where ^{40}K decay dominates. This relation is consistent as can be seen by the different runs that overlap. The bottom graph shows how the exponential slope is effected by the multiplicity. The correlation is as expected since there should be no depth dependence for multiplicities where ^{40}K decay is the primary source of signal. Atmospheric muons are assumed to become the dominant source at multiplicity 8, as expected, after that, the slope becomes consistent therewith. Because the rate of the higher multiplicities is lower there is less data and this increases the uncertainty, this causes the value of the exponential slope to differ at higher multiplicities. The multiplicity is also used to determine the validity of the used method. This is done by analysing the data for multiplicity 4, since there should be no seasonal variation in the ^{40}K decay. If the rate

at multiplicity 4 is consistent during the measuring period it shows that the analyses works as expected.

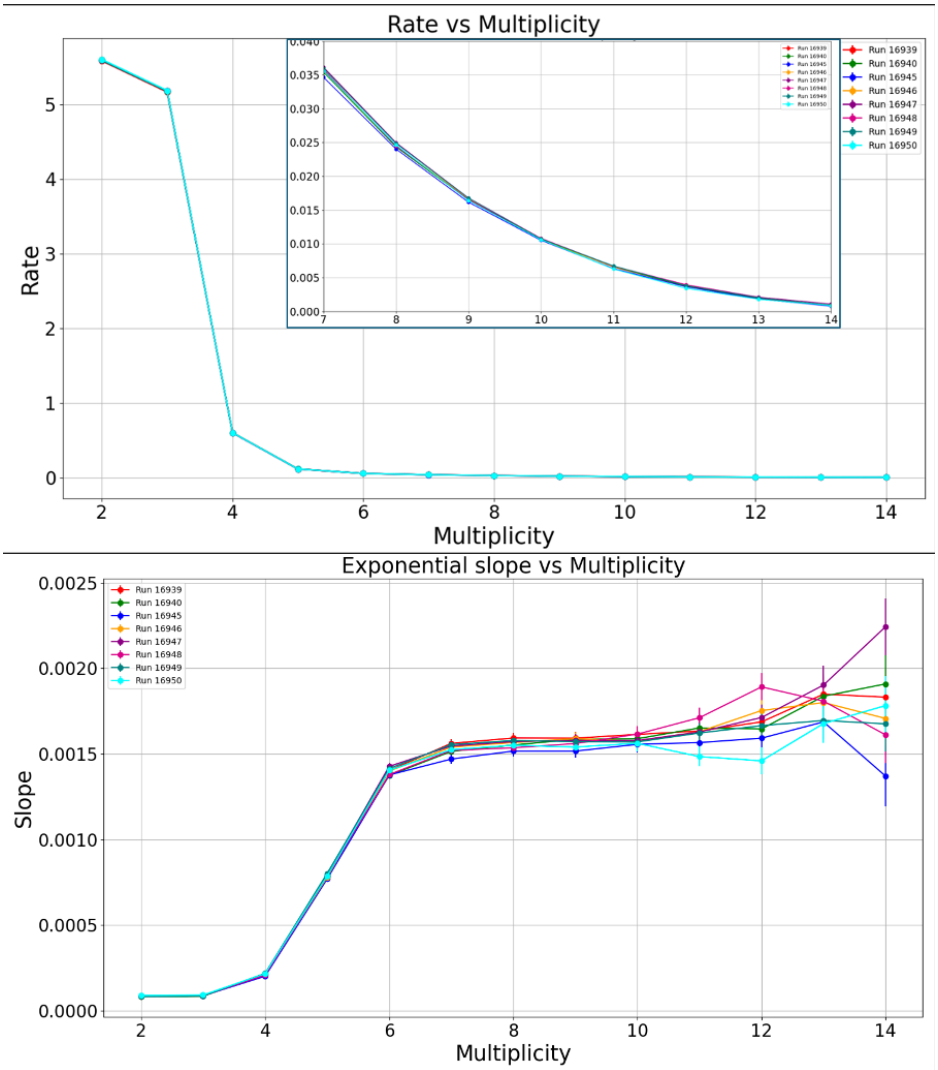

Figure 5.1: *The rate (top) and exponential slope (bottom) for multiplicities 2 to 14 for 10 different runs each depicted with a different colour. The dominance of the ^{40}K decay on the rate (Hz) at 2740 meters can be seen in the low multiplicities, this shows the importance of the multiplicity cut for the analysis. The inset is zoomed in on multiplicities 7 to 14 to show the effect of the higher multiplicities on the rate. The bottom graph shows the effect on the exponential fit parameter, because the ^{40}K decay can be considered as depth independent, the slope is approximately 0 at low multiplicity.*

5.2 Coincidence Count

Since the runtime for every DOM from every DU is recorded, the first step is to determine the coincidence count for each run. As mentioned above, for the analysis, the coincidence count that is used is for multiplicities of 8 and higher, multiplicity 4 is used to validate the method. The coincidence count is linearly dependent of the runtime, thus if there are large differences in the coincidence count compared to the runtime, it indicates there is some other factor that influenced the results. The raw coincidence count for the measuring period for DU 27 is illustrated in figure 5.2.

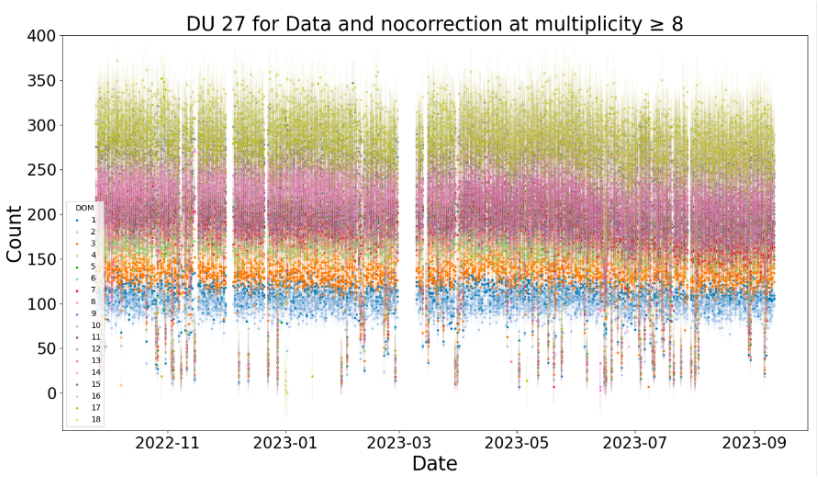

Figure 5.2: *The raw coincidence count for the measuring period for DU 27. Each colour represents a different DOM, as indicated in the legend.*

5.3 Runtime

To determine the rate, the coincidence count is divided by the runtime. The runtime can vary per run per DOM; to take this into account, the rate is determined per DOM by dividing the DOM specific coincidence count by the DOM specific runtime. The runtime for DU 27 can be seen in figure 5.3. From the runtime analysis, it becomes clear that DOM 6 was turned off for the measuring period. It can also be seen that there is a gap in the data in the beginning of March. This gap is present due to the quality cuts that are performed on the raw data, this resulted in a period where no data was available. The instances where certain DOMs have lower runtimes is due to HRV, as explained in the Bioluminescence section.

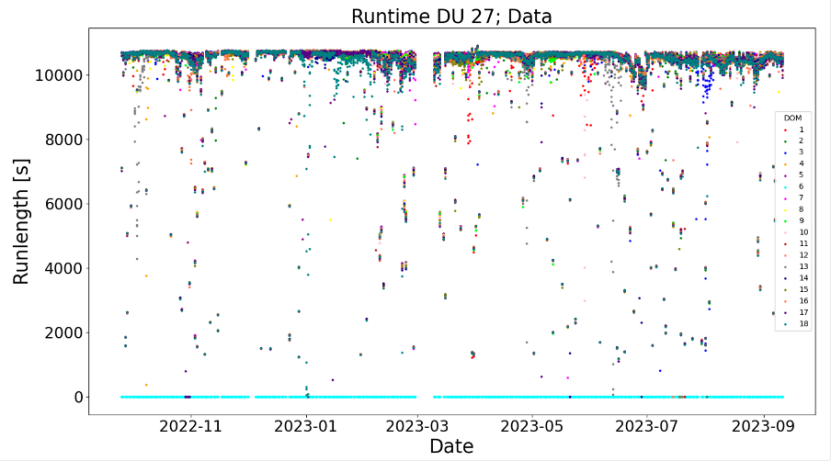

Figure 5.3: *The runtime for every DOM for DU 27 over the measuring period used in the analysis.*

When comparing figure 5.2 with figure 5.3, it would be expected to see the same line for DOM 6. The reason DOM 6 is not in figure 5.2 is because for the coincidence count and rate analyses results of 0 are removed. This is to ensure that the fit parameter and rate determined at 2740 meters deep, with the use of depth dependence, is not affected. The runtime is consistent over the entire period, even though the rate is determined per DOM for its specific runtime, for the analysis it is best to minimize the number of variables. The consistency of the runtimes decreases the chance that it affects the end result.

5.4 Efficiency

After the rate has been determined it has to be corrected for DOM efficiencies using the PMT efficiencies. Figure 5.4 shows the efficiency for every PMT in a single run and the DOM efficiency that is calculated from it*. This graph also shows that for DOM 6 the efficiency is 0, and is therefore excluded from further analysis. This is what is expected because the DOM was turned off, also showing that the system for determining the efficiencies works.

*How the DOM efficiency is determined can be found in chapter 4.1.3.

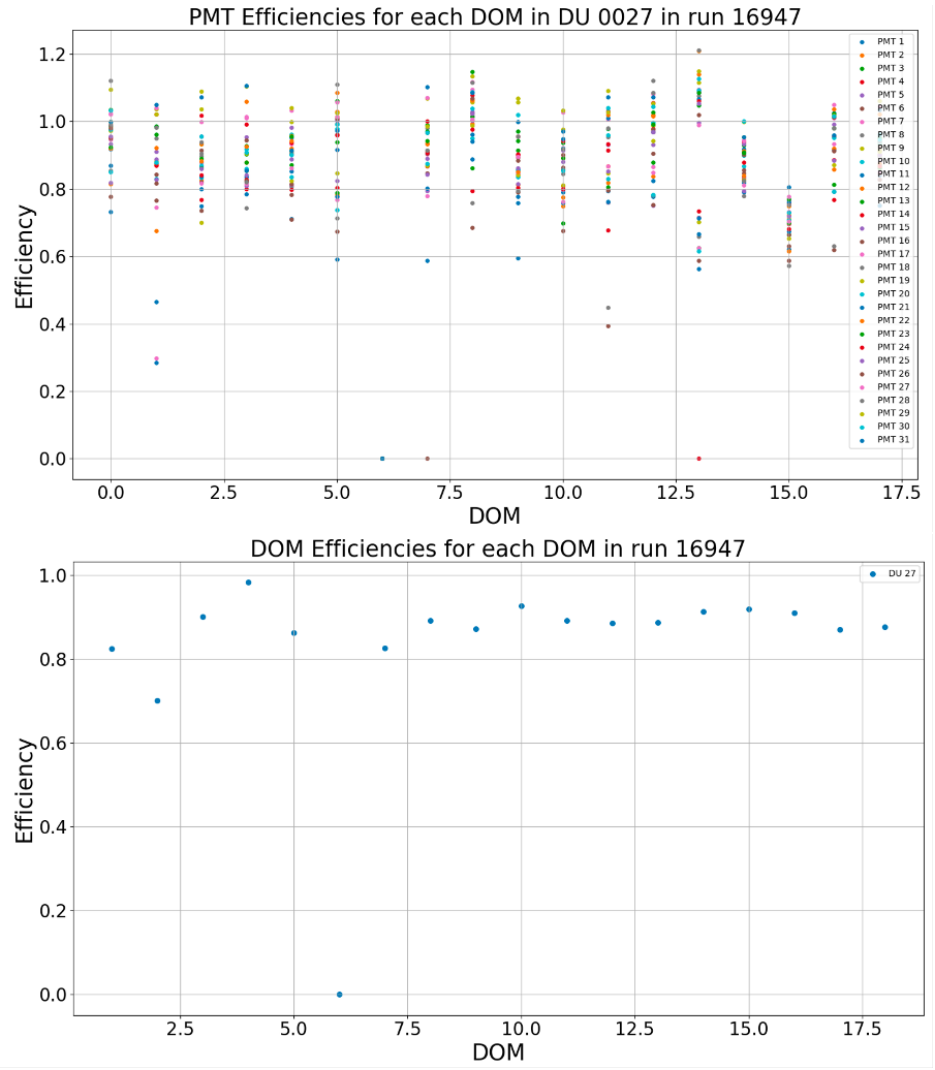

Figure 5.4: *Top: The efficiency of every PMT in DU 27 for run 16947. Bottom: The PMT efficiency combined into a DOM efficiency for DU 27.*

Figure 5.5 shows the result of this process over the entire period. What stands out is that the efficiency of nearly every DOM decreases. This is caused by sediment collecting on the outside of the DOMs. The efficiency as a function of the date of all DUs can be seen in the appendix. While this decrease is noteworthy, it should not affect the final result because the efficiency correction is applied per DOM per RUN. This ensures a proportional correction for the entire measuring period despite the change in efficiency.

The best way to show the effect of the efficiency correction on the data

is to compare the data that is not efficiency corrected with data that is, this can be seen in figure 5.6. What stands out is the efficiency corrected rate increases by approximately 0.05 for all the DOMs, the outliers in the lowest and highest rate DOMs are also reduced. This can be seen by the frequency they occur and the distance between the outliers and the rest of data points. Figure 5.6 also shows that the the decrease in rate between May and September of 2023 is partially compensated by the efficiency correction, it, however, does not remove it entirely.

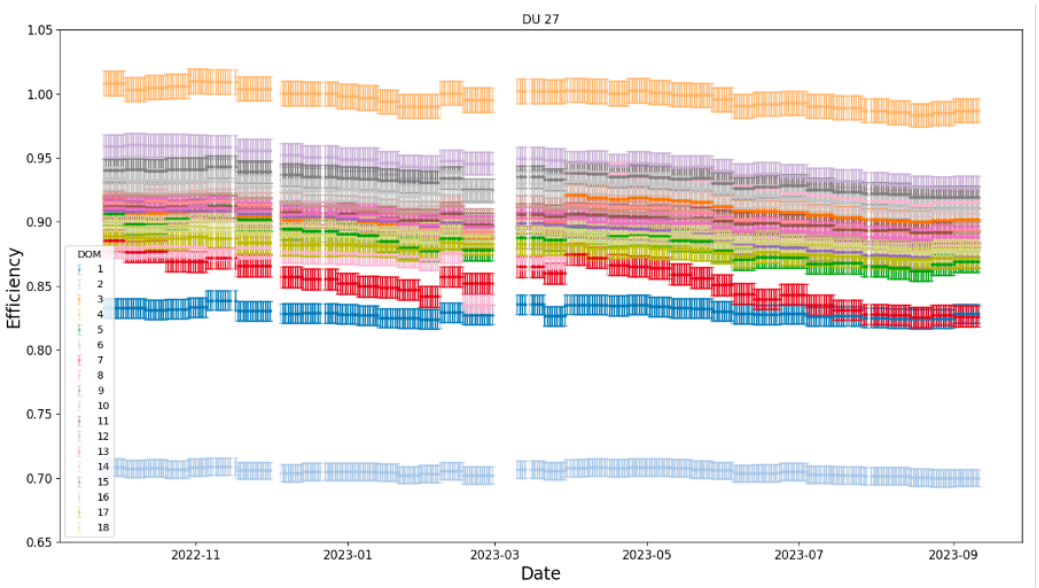

Figure 5.5: *DOM efficiency with its respective error for DU 27 as a function of the date. The plot has been limited on the Y-axis due to DOM 6 having efficiency 0.*

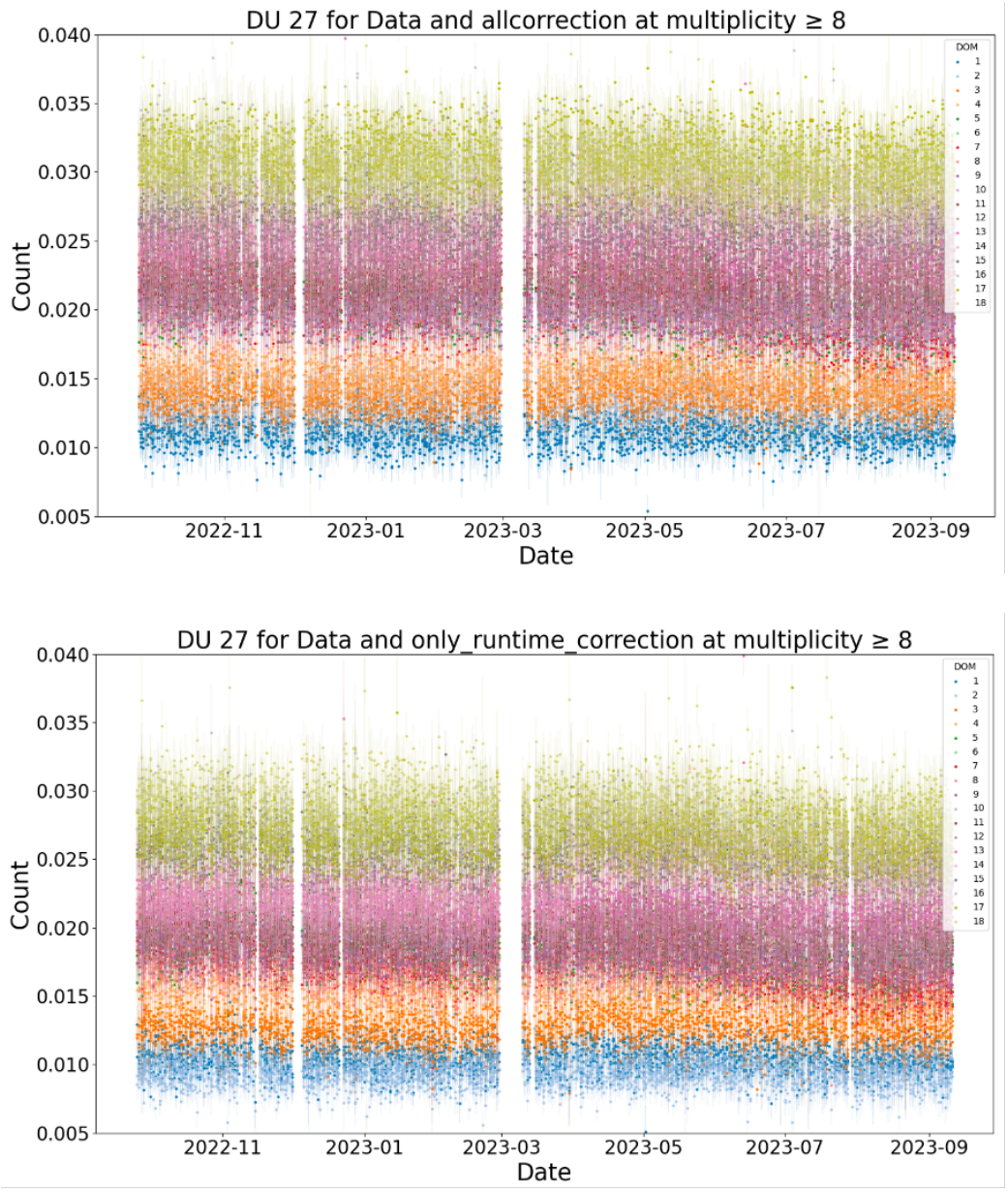

Figure 5.6: *Top: The rate for every DOM in DU 27 corrected for efficiency and runtime as a function of the date. Bottom: The rate for every DOM in DU 27 corrected for the runtime as a function of the date. Both for multiplicity equal to or larger than 8. Each colour represents the data collected by a certain DOM, as indicated in the legend.*

5.5 DU selection

The next step in the analysis is to assess the performance of the DUs, determining which will be selected for the final analysis. This is done because multiple variables can affect the DU specific rate, this could lead to a single DOM having a large effect on the final rate determination. The method used determines the rate and exponential fit parameter for every run. This is plotted as a function of run number, this is shown in figure 5.7.

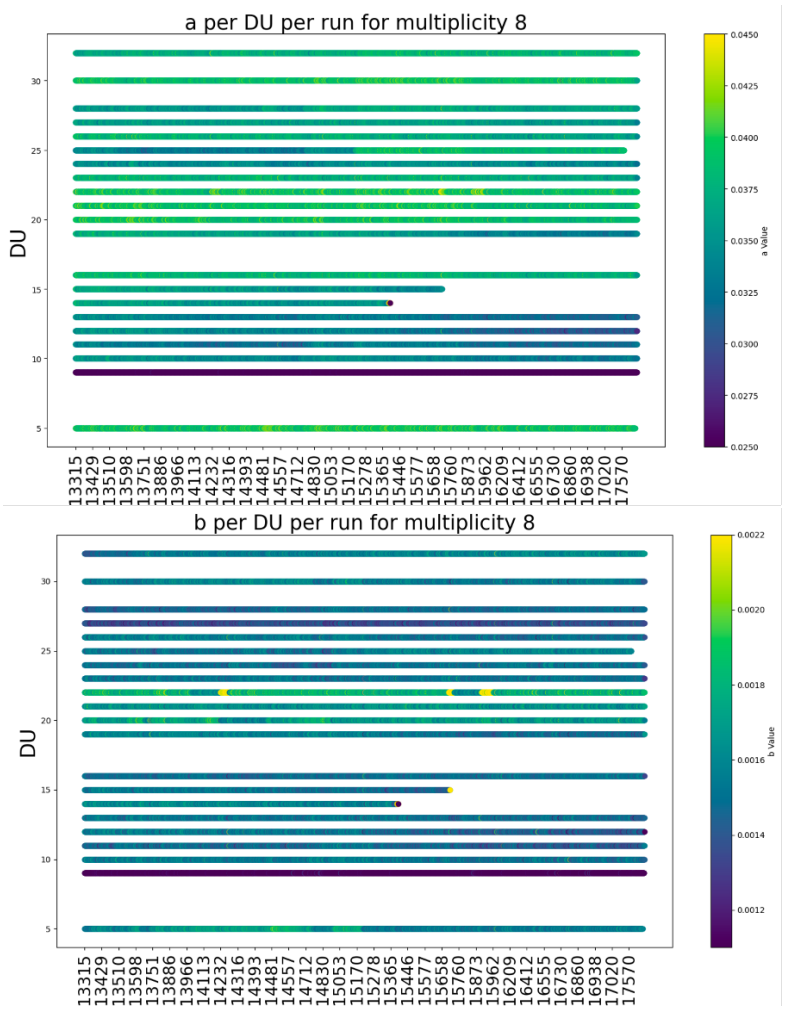

Figure 5.7: *Top: The value for a, which is the rate at 2740 meters, for every operational DU for every run. Bottom: The value for b, which is a fit parameter that represents the exponential slope of the depth dependence, for every operational DU for every run.*

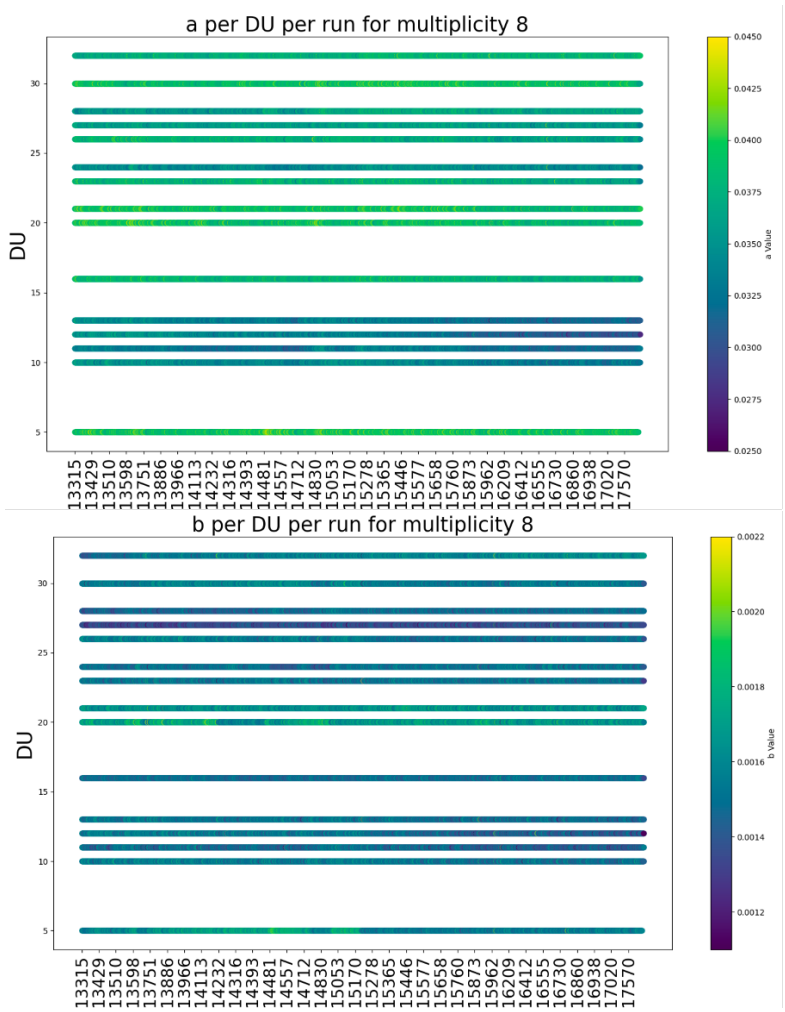

Figure 5.8: *Top: The value for a, which is the rate at 2740 meters, for the selected DUs for every run. Bottom: The value for b, which is a fit parameter that represents the exponential slope of the depth dependence, the selected DUs for every run.*

The decision was made to exclude DU 9, DU 14, DU 15, DU 19, and DU 22 in the final analysis. DU 9 due to known issues with determining the efficiency accurately, this is a known problem of this DU, probably caused by a defect in the optical gel. DU 14 and DU 15 were not operational for a notable period, this results in their exclusion. DU 19 showed a steady decrease in rate, it was excluded due to there not being a apparent cause. The data collected by DU 22 has not been used because of the runs where the exponential slope substantially increased. The rate DU 25 measured consists of two consistent periods; because no explanation has been found for

the sudden increase, it was excluded. Figure 5.8 shows the rate and exponential slope of the final selection of DUs. From DU 23 DOM 12 has been excluded, this is due to problems with establishing an accurate efficiency, this can be seen in figure 5.9.

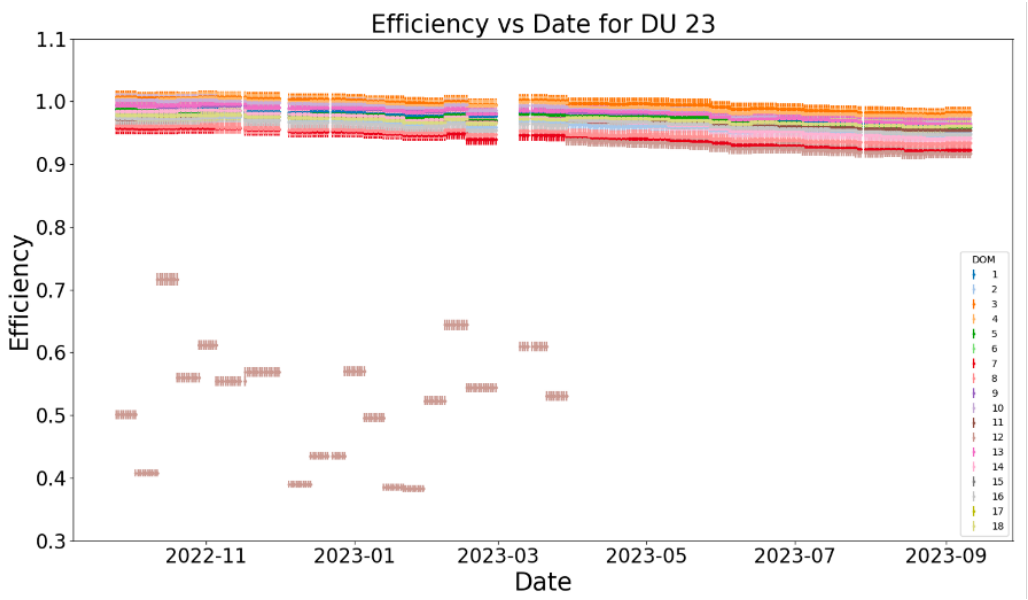

Figure 5.9: *Efficiency as a function of date for DU 23, the efficiency of DOM 12 is inconsistent, resulting in its exclusion from the analysis.*

Another thing that stood out in figure 5.8, is that the DUs 10, 11, 12, and 13 have a significantly lower rate than the other DUs. This is most likely due to the efficiency correction because these DUs also have notably lower efficiency, as can be seen in the appendix.

5.6 Rate and Slope over Time

To be able to draw a comparison between temperature and rate, the daily average rate needs to be calculated. This is because the measurements of the temperature and runs made at the same time. To determine the daily average of both the rate and exponential slope, the mean is used, this can be seen in figure 5.10.

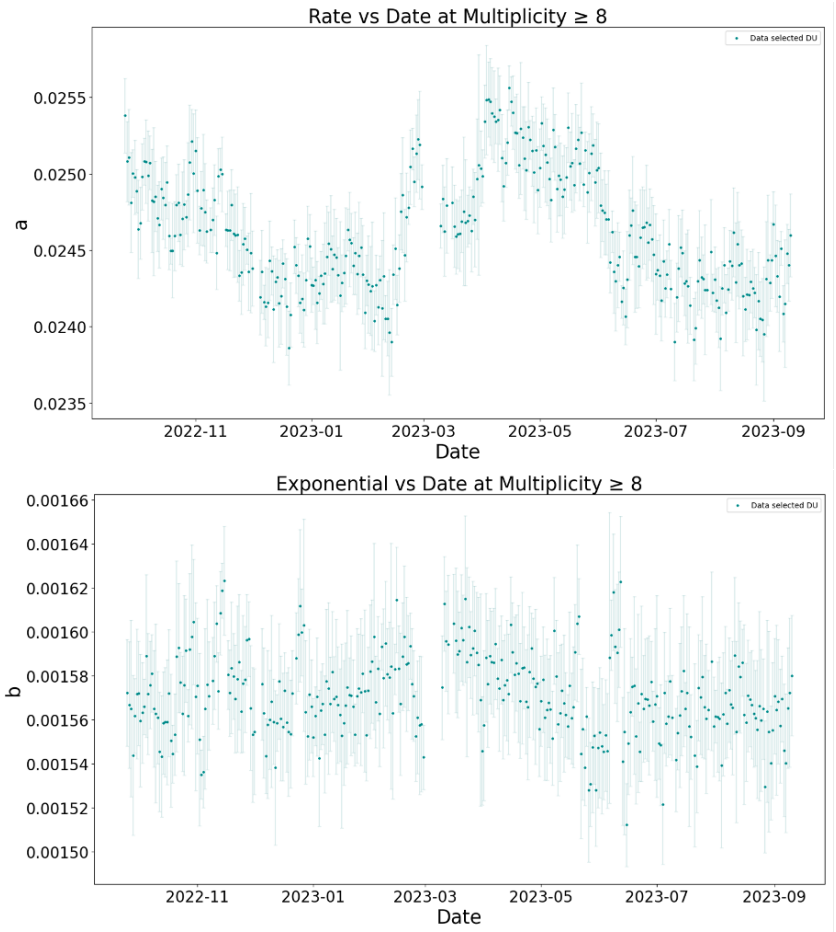

Figure 5.10: *Top: The daily average rate over the entire period for the selected DUs. Bottom: The daily average exponential slope. Both for multiplicity equal or greater than 8.*

What is most notable is the approximate 5% decrease in rate starting in May; as in May the temperature starts to rise, it is expected for the rate to increase. A similar trend can be seen in the exponential slope, since this only depicts the depth dependence, a seasonal correlation was not expected. This decrease affects the final analysis in multiple ways, since the relative rate $\Delta a / \langle a \rangle$ is used. This means each Δa is compared to the average rate of the entire period, however the differences in rate are only a few percent. Because of the size of these differences, the affected average does not have a big influence on the end result.

Searching for a possible cause of this decrease, the same analysis was performed on data of multiplicity 4; if this showed the same trend, this could be a sign that the problem lies in the analysis. This is shown in figure

5.11, since there is no seasonal variation in ^{40}K decay, the rate should be constant. The large fluctuations indicate that the analysis is still flawed and that there may be systematics still not properly accounted for. Figure 5.11 also shows a decrease in the rate starting in May. However, due to the fluctuations and sudden increases and decreases it is unreliable as an indicator of the actual trend.

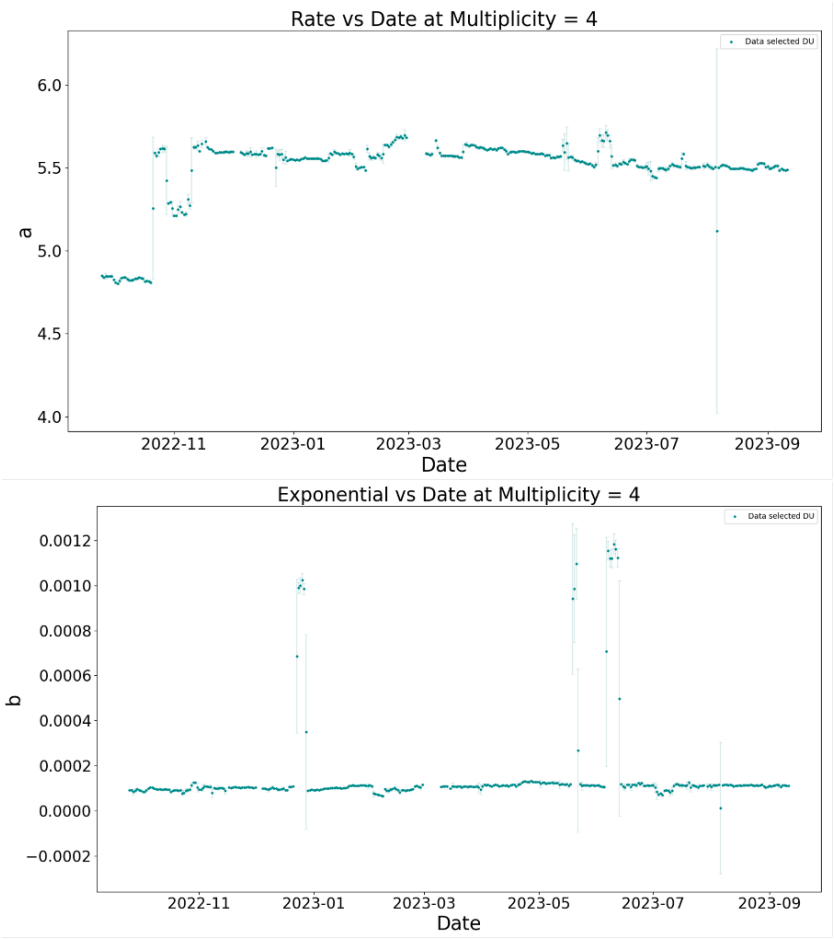

Figure 5.11: *Top: The daily average rate over the entire period for the selected DUs. Bottom: The daily average exponential slope. Both for multiplicity 4.*

5.7 Relative Rate

The final step of the rate analysis is determining the relative rate, $\Delta a / \langle a \rangle$. Combining aforementioned methods resulted in the relative rate in figure 5.12. As expected, it shows the same trend as the daily average rate.

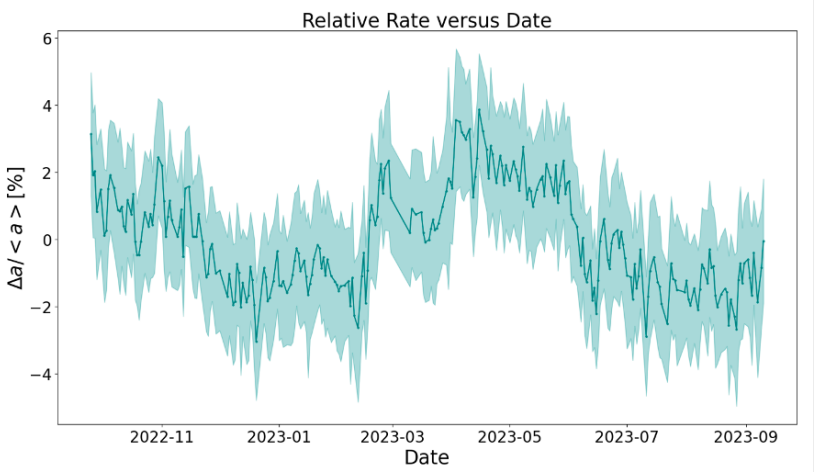

Figure 5.12: *The relative rate as a function of the date, most notable the decrease in rate after May 2023.*

Chapter 6

Temperature Analysis

The data collected by NASA's AIRS mission is analysed to establish the daily average temperature over the measuring period, as can be seen in figure 6.1. As expected, the temperature decreases from September until February, then it increases steadily. The daily average temperature is a weighted average taken over different heights, where the top of the atmosphere is most heavily weighted. The largest fluctuations are present in the months July and August. Due to the distribution of the weights, these are probably caused by temperature changes in the stratosphere. These changes can have multiple sources, such as tropospheric weather patterns, where storms, heatwaves, and cold fronts influence the temperature of the stratosphere through vertical transport of energy or momentum. Other possible sources include atmospheric waves that propagate from the troposphere into the stratosphere to influence the temperature [2].

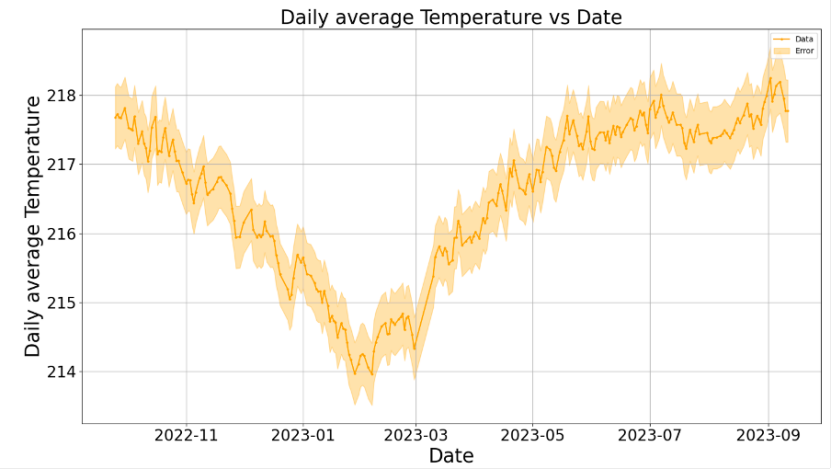

Figure 6.1: *Temperature as a function of the date, the average of the two daily measurements is calculated to determine the daily average effective temperature. The temperature varies between a low of* $\approx 214K$ *and a high of* $\approx 218K$.

In the final analysis the effective temperature $\Delta T_{eff} / \langle T_{eff} \rangle$ is compared to the relative rate. The effective temperature can be seen in figure 6.2. The expected temperature change is about was approximately 4%, this is higher than found over this period.

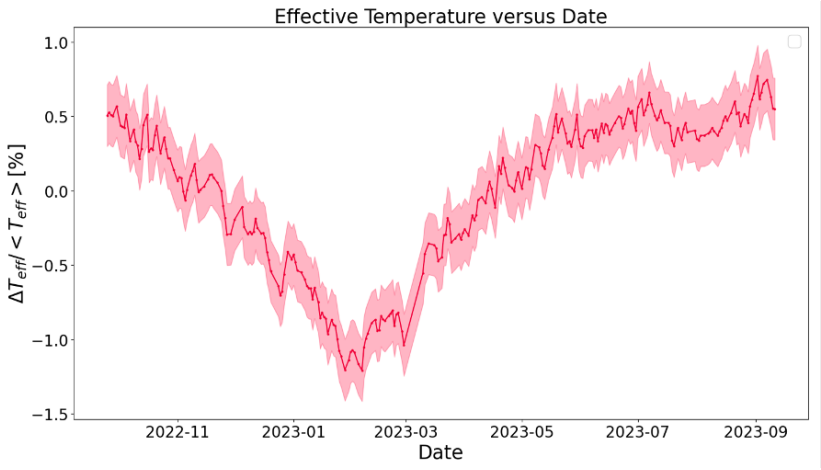

Figure 6.2: *Effective temperature as a function of the date*

Chapter 7

Results

By combining the rate and temperature analysis, α_T can be determined since it is the linear coefficient between them. Figure 7.1 shows the relative rate and relative temperature over the measuring period. Most notable is the period from May to September where the relative rate and effective temperature follow different trends. This is especially apparent since before May they do follow the same trend.

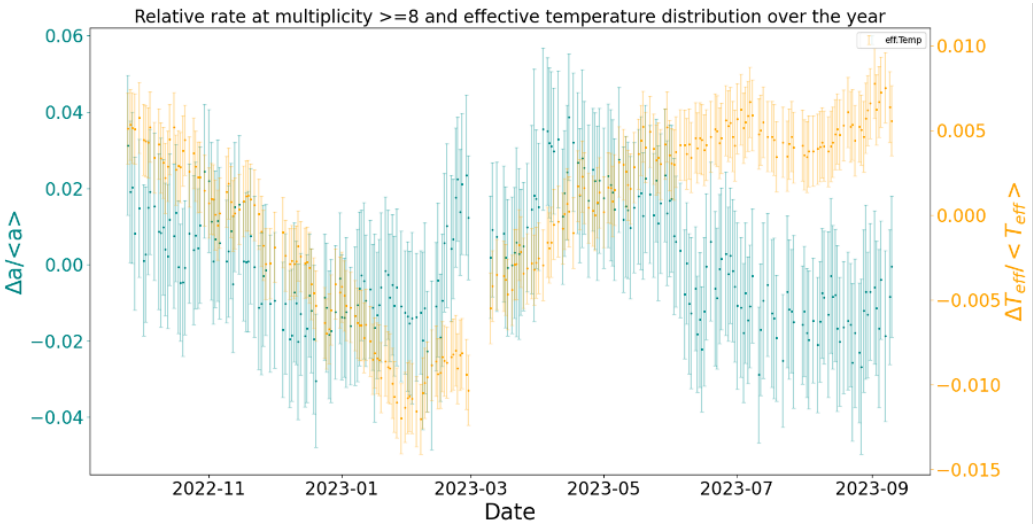

Figure 7.1: *The relative rate (left) and effective temperature (right) as functions of the date.*

Figure 7.2 shows the relative rate as a function of the effective temperature for multiplicity equal or larger than 8. This resulted in a $\alpha_T = 0.227 \pm 0.179$ and is obtained by determining the slope of the linear fit of

the relative rate as a function of the effective temperature. What is most notable in this figure is the group of data points with low relative rate and high effective temperature, this group is also apparent in figures 7.3 and 7.4. These points have a large effect on the final fit and originate from the period May to September, where the rate decreases while the temperature rises. Figure 7.5 still shows this group of data points but the increased multiplicity decreased the effect. This also results in $\alpha_T = 0.591 \pm 0.215$, this is closer to the predicted value of 0.86.

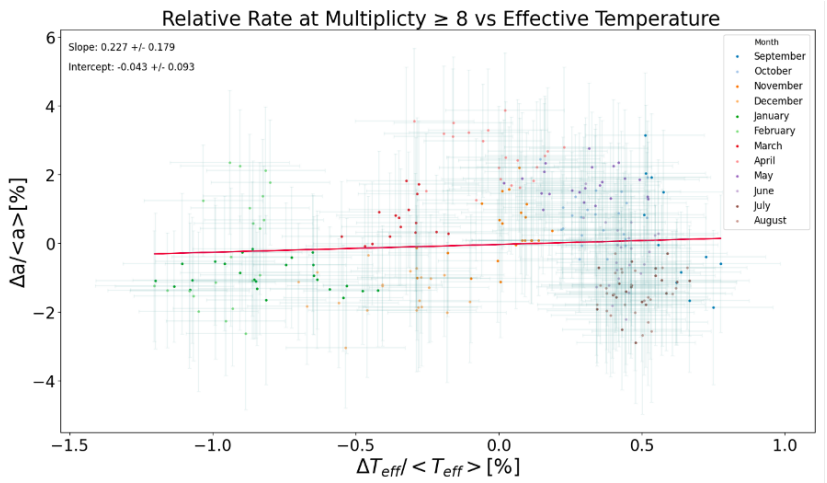

Figure 7.2: *The relative rate as a function of the effective temperature for multiplicity larger or equal to 8.* $\alpha_T = 0.227 \pm 0.179$.

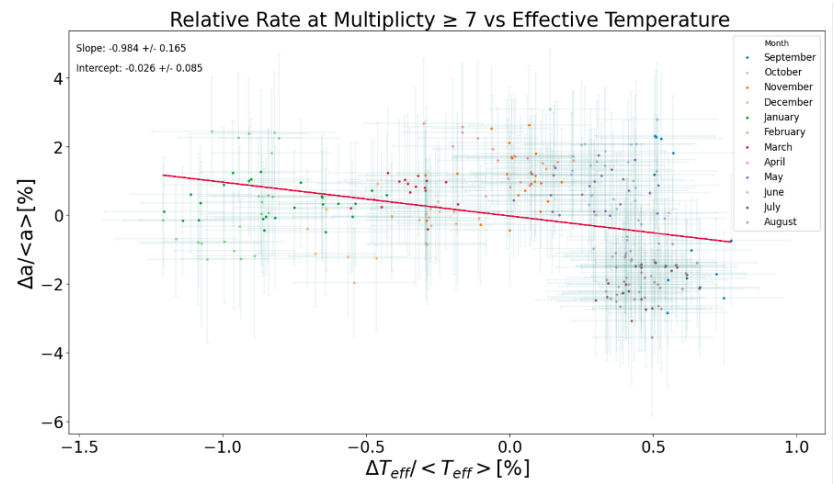

Figure 7.3: *The relative rate as a function of the effective temperature for multiplicity larger or equal to 7.* $\alpha_T = -0.984 \pm 0.0.165$.

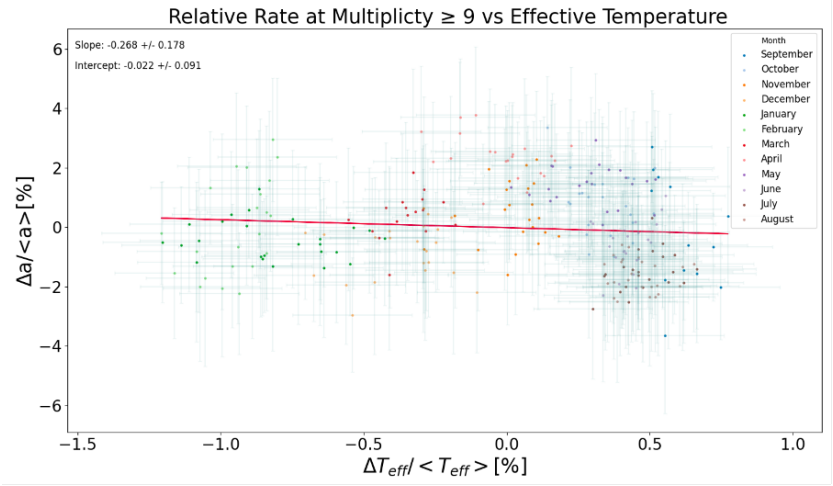

Figure 7.4: *The relative rate as a function of the effective temperature for multiplicity larger or equal to 9.* $\alpha_T = -0.268 \pm 0.178$.

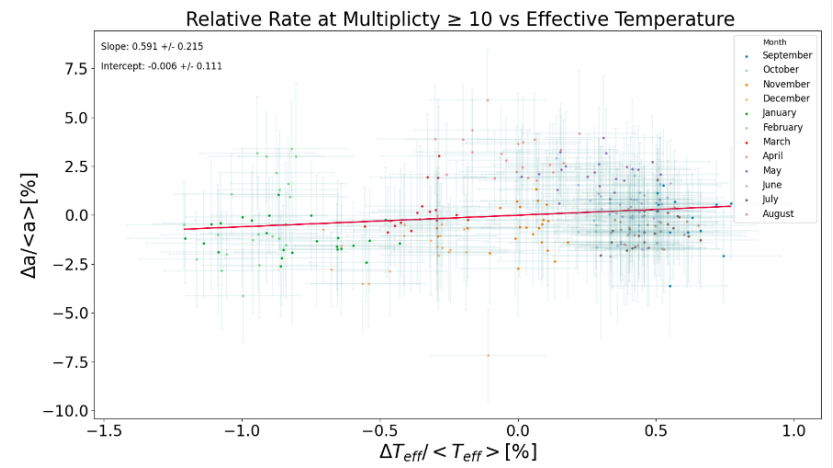

Figure 7.5: *The relative rate as a function of the effective temperature for multiplicity larger or equal to 10.* $\alpha_T = 0.591 \pm 0.215$.

In order to assess the correlation, the data has been limited to the period from September to May, this results in $\alpha_T = 1.800 \pm 0.191$, as can be seen in figure 7.6. This is a result more in line with the predictions and previous research, that is why it was chosen as the final result. This can be seen as an indicator that an error is present in the analysis that causes the decrease in rate in the second half of the measuring period. As another validity check, the relative exponential, β_T, as a function of the effective temperature can be seen in figure 7.7, both for the whole measuring pe-

riod and the selection from September to May. No seasonal correlation was hypothesized between the relative exponential and effective temperature. However, a negative correlation of $\beta_T = -0.568 \pm 0.139$ over the entire period and $\beta_T = -0.446 \pm 0.187$ over the selected period is found. What is notable is that the group of data points from the period that is filtered out are situated exclusively near the low relative exponential and high effective temperature. The effect this group of points has on the value of β_T, is however much less than for the relative rate. The negative correlation could originate from factors such as atmospheric density or density variations affecting the muon creation resulting in a reduced depth dependence when temperature increases. However, this has not been properly examined in this research so no definitive conclusions can be drawn.

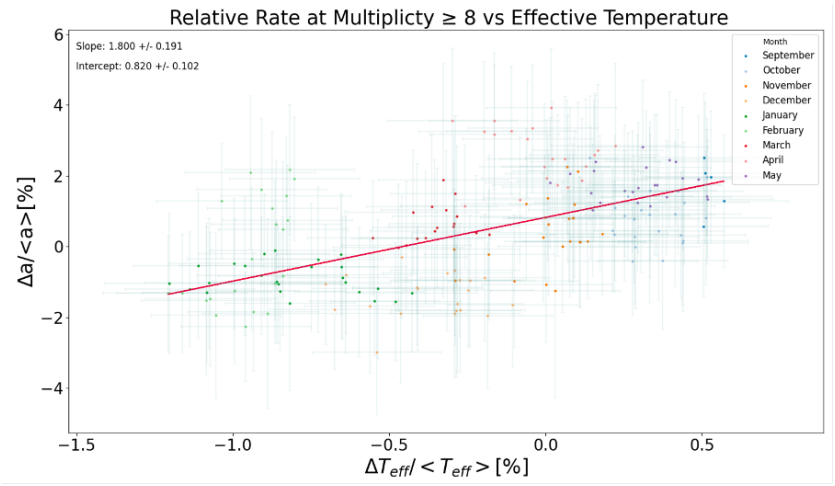

Figure 7.6: *The relative rate as a function of the effective temperature for multiplicity larger or equal to 8 over the period from September to May. The slope is* 1.800 ± 0.191.

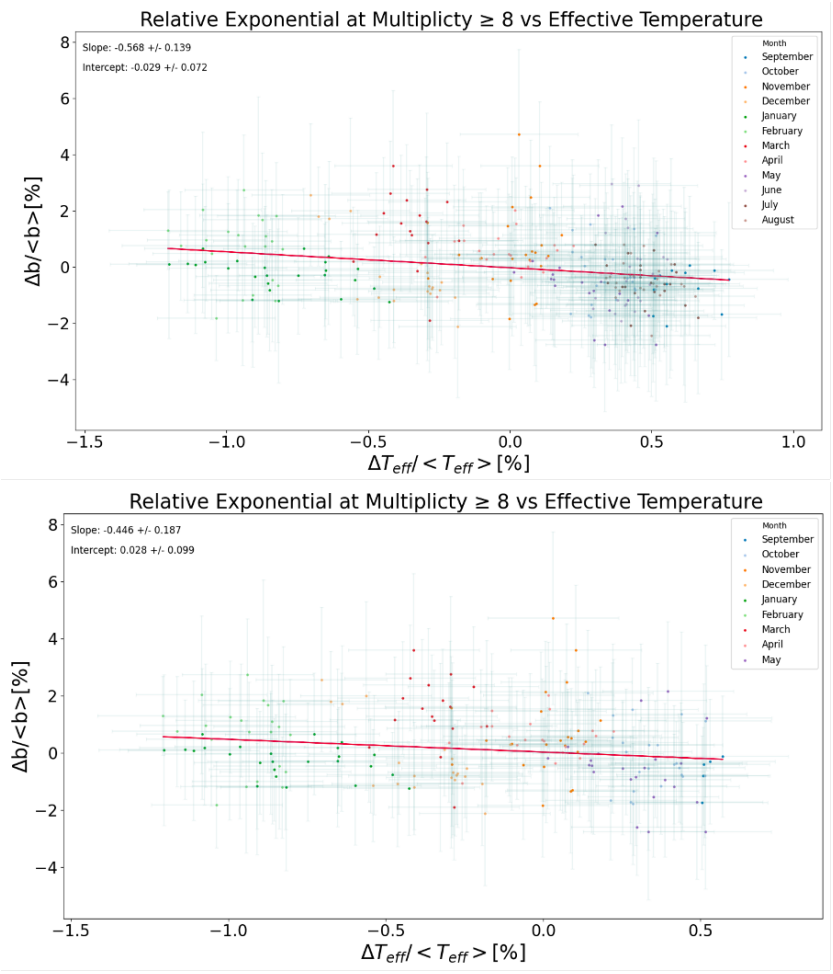

Figure 7.7: *Top: Relative exponential slope as a function of the effective temperature for multiplicity larger or equal to 8 for the whole measuring period. Bottom: Relative exponential slope as a function of the effective temperature for multiplicity equal to 8 for the selected measuring period.*

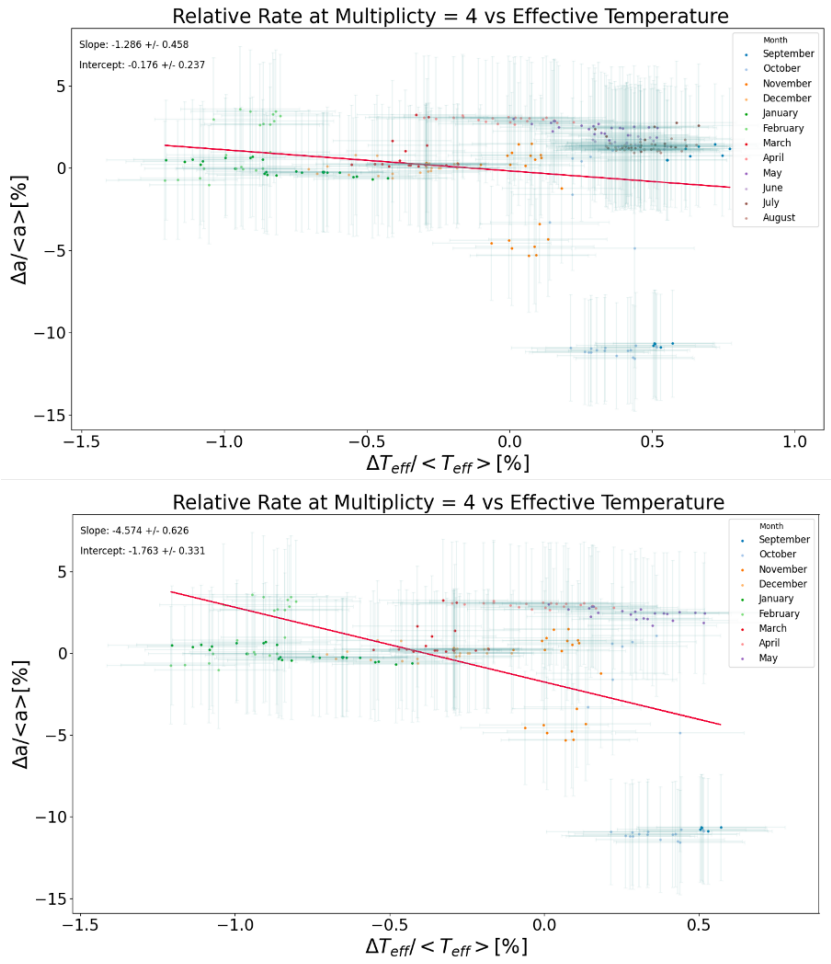

Figure 7.8: *Top: Relative rate as a function of the effective temperature for multiplicity equal to 4 for the whole measuring period. Bottom: Relative rate as a function of the effective temperature for multiplicity larger of equal to 4 for the selected measuring period.*

The last validity check performed is determining α_T for multiplicity 4; since this data is dominated by ^{40}K decay, there should be no correlation as can be seen in figure 7.8. A negative correlation is present over the whole and selected period of respectively $\alpha_T = -1.286 \pm 0.458$ and $\alpha_T = -4.574 \pm 0.626$. This is another indicator that the analysis is still flawed and improvements can be made to determine a more accurate correlation between the relative rate and effective temperature. However, the overall results support the notion of a seasonal variation in the muon rate.

Chapter 8

Discussion

The most important factor influencing the final results has been the decrease in rate starting from May. This is most probably caused by the efficiency correction which does not seem to be functioning as intended. This led to findings that were not consistent with the expectations or previous research unless a cut was performed on the data, excluding the measuring period from May to September. There are multiple figures that show this; in figure 5.8, the DUs with lower efficiency also show a significantly lower rate. Figure 7.1 shows a decrease in rate while the rate should increase with increasing temperature. The difference in α_T over the entire period and the selected period can be seen by comparing figure 7.2 to figure 7.6. The decrease observed in efficiency from May to September for every DU, as demonstrated in the appendix, aligns with the concurrent decrease in rate, indicating that the problem lies with the assumed relationship between the DOM efficiency and the rate, which can be seen in figure 4.3. Improvements lie in how the efficiency correction is used to compensate for steadily decreasing PMT efficiencies. Improving this correction removes obstacles when determining α_T over longer periods.

Additionally, figure 7.8 indicates that there are still other variables that affect the relative rate due to the groups of data points with a significantly lower relative rate and a high effective temperature. This indicates that the rate establishment still needs to be improved. This combined with the negative correlation between the relative exponential slope and the effective temperature shows that there are other effects that influence the rate.

The α_T determined over the selected period is equal to 1.800 ± 0.191, this is higher than the expected value of 0.86. Previous research found $\alpha_T = 1.166 \pm 0.128$ for the ARCA detector [24] and $\alpha_T = 1.005 \pm 0.041$

[19]. Both these studies also found higher values than the predicted value for α_T. That the α_T at ARCA is higher than at ORCA is expected since it is located at greater depth, as established in figure 2.6.

The final notable result found is the spread in the data points in figure 7.6, this indicates there are still systematics unaccounted for. This can be improved in both the relative rate establishment and the effective temperature, this is partly due to both variables being daily averages. The main aspect that needs to be improved to improve the determination of α_T is the efficiency correction. This will allow the use of longer periods of data.

Chapter 9

Conclusion

Based on the comprehensive rate and temperature analyses conducted, several key findings have emerged, shedding light on the behavior of the ARCA KM3NeT detector and the correlation between atmospheric muon rate and the effective temperature.

The multiplicity analysis showed the impact of multiplicity on the measured rate. Notably, the ^{40}K decay dominance at lower multiplicities and atmospheric muon signals at higher multiplicities. This analysis also served as a validation of the methodology, as it showed consistency in rate measurements across different multiplicities.

Moving on to the coincidence count and runtime analyses, the linear dependence of coincidence count on runtime combined with differing runtimes for certain DOMs, shows the importance in accounting for runtime variations when calculating rates per DOM. The stability and consistency of the runtime data showed throughout the measuring period further confirm the reliability of the analysis.

The efficiency variations illustrated in figure 5.4 across DOMs emphasise the importance of correcting for these variations to obtain accurate rates. Notably, the correction significantly influenced rate values, showing the necessity of this step in ensuring data integrity even more.

DU selection emphasized the importance of evaluating DU performance and excluding DUs that showed unexplained behavior to prevent bias in the final rate determination. This careful selection process ensured robustness and reliability in the subsequent analyses.

The temperature analysis in Chapter 6 provide valuable insights into atmospheric temperature trends and their potential impact on muon rates. Notably, the observed temperature variations over the measuring period provided context for interpreting rate fluctuations and assessing their cor-

Version of June 13, 2024– Created June 13, 2024 - 15:36

relation with atmospheric conditions.

Finally, the results chapter combines the findings from both rate and temperature analyses to determine the temperature coefficient $\alpha_T = 1.800 \pm 0.191$. The comparison of relative rate and temperature revealed a strong correlation, albeit with unexpected trends in certain periods. While the determined α_T values deviated from theoretical predictions, they aligned with previous research findings for the ARCA detector, indicating consistency and reliability of the results.

Overall, the analysis offers valuable insights into the behaviour of the ARCA KM3NeT detector and its relationship with atmospheric conditions. The correlations and trends found pave the way for further research and improvements in methodology to enhance the accuracy of future analyses.

Version of June 13, 2024– Created June 13, 2024 - 15:36

Bibliography

[1] P. Adamson and Andreopoulos. Observation of muon intensity variations by season with the minos far detector. *Physical Review D*, 81(1), January 2010.

[2] LAURA CIASTO AMY BUTLER. The stratosphere is talking down to the troposphere, but will it listen?

[3] J.L. Autran, D. Munteanu, T. Saad Saoud, and S. Moindjie. Characterization of atmospheric muons at sea level using a cosmic ray telescope. *Nuclear Instruments and Methods in Physics Research Section A: Accelerators, Spectrometers, Detectors and Associated Equipment*, 903:77–84, 2018.

[4] Paul H. Barrett, Lowell M. Bollinger, Giuseppe Cocconi, Yehuda Eisenberg, and Kennet Greisen. Interpretation of Cosmic-Ray Measurements Far Underground. *Rev. Mod. Phys*, 24:133–178, 1952.

[5] J. Beringer, J. F. Arguin, and Barnett. Review of particle physics. *Phys. Rev. D*, 86:010001, Jul 2012.

[6] E. V. Bugaev, A. Misaki, V. A. Naumov, T. S. Sinegovskaya, S. I. Sinegovsky, and N. Takahashi. Atmospheric muon flux at sea level, underground, and underwater. *Physical Review D*, 58(5), July 1998.

[7] Stefano Cecchini and Maurizio Spurio. Atmospheric muons: experimental aspects, 2012.

[8] Luke O'C. Drury. Origin of cosmic rays. *Astroparticle Physics*, 39-40:52–60, 2012. Cosmic Rays Topical Issue.

[9] Klaus Geyer. *Measurements of the atmospheric muon rate with the ANTARES neutrino telescope*. PhD thesis, Erlangen - Nuremberg U., 2015.

[10] E.W. Grashorn, J.K. de Jong, M.C. Goodman, A. Habig, and Marshak. The atmospheric charged kaon/pion ratio using seasonal variation methods. *Astroparticle Physics*, 33(3):140â145, April 2010.

[11] Peter K.F. Grieder. Chapter 2 - cosmic rays in the atmosphere. In Peter K.F. Grieder, editor, *Cosmic Rays at Earth*, pages 55–303. Elsevier, Amsterdam, 2001.

[12] Claus Grupen. *Astroparticle Physics*. Springer, Berlin, Heidelberg, 2005.

[13] Andreas Haungs, Dongyun Kang, and Schoo. "the kascade cosmic-ray data centre kcdc: Granting open access to astroparticle physics research data". 06 2018.

[14] Victor Hess. Nobel Prize for Physics: Prof. Victor F. Hess. *Nature*, 138:873, 1936.

[15] A. M. Hillas. Cosmic rays: Recent progress and some current questions, 2006.

[16] Li Zhili Wetzel Benjamin Hu, Yi. Cherenkov radiation control via self-accelerating wave-packets. *Scientific Reports*, 7, 08 2017.

[17] Lulu Liu and Pablo Solis. The speed and lifetime of cosmic ray muons. 2007.

[18] F. Ameli M. Andre M. Ageron, S. Aiello. Dependence of atmospheric muon flux on seawater depth measured with the first km3net detection units. 02 2020.

[19] Jelmer Mulder and Ronald Bruijn. Seasonal variation of the atmopsheric muon flux in the KM3NeT detectors. *PoS*, ICRC2023:355, 2023.

[20] Seth H. Neddermeyer and Carl D. Anderson. Note on the Nature of Cosmic-Ray Particles. *Phys. Rev.*, 51:884–886, 1937.

[21] A. Palladino, G. Pagliaroli, F. L. Villante, and F. Vissani. What is the flavor of the cosmic neutrinos seen by icecube? *Phys. Rev. Lett.*, 114:171101, Apr 2015.

[22] Wolfgang Pauli. Dear radioactive ladies and gentlemen.

[23] B. Resnick. Extremely powerful cosmic rays are rainign down on us. no one knows where they come from.

[24] Lara Skarbal. Seasonal Variation of the Atmospheric Muon Flux at KM3NeT. 2024.

Chapter 10

appendix

10.1 Error in DOM Efficiency

$$\Delta E_{DOM} = \frac{\sqrt{\sum_{i=0}^{30}(w_i \Delta E_i)^2}}{\sum_{i=0}^{30} w_i} \tag{10.1}$$

10.2 DU Efficiencies

Version of June 13, 2024– Created June 13, 2024 - 15:36

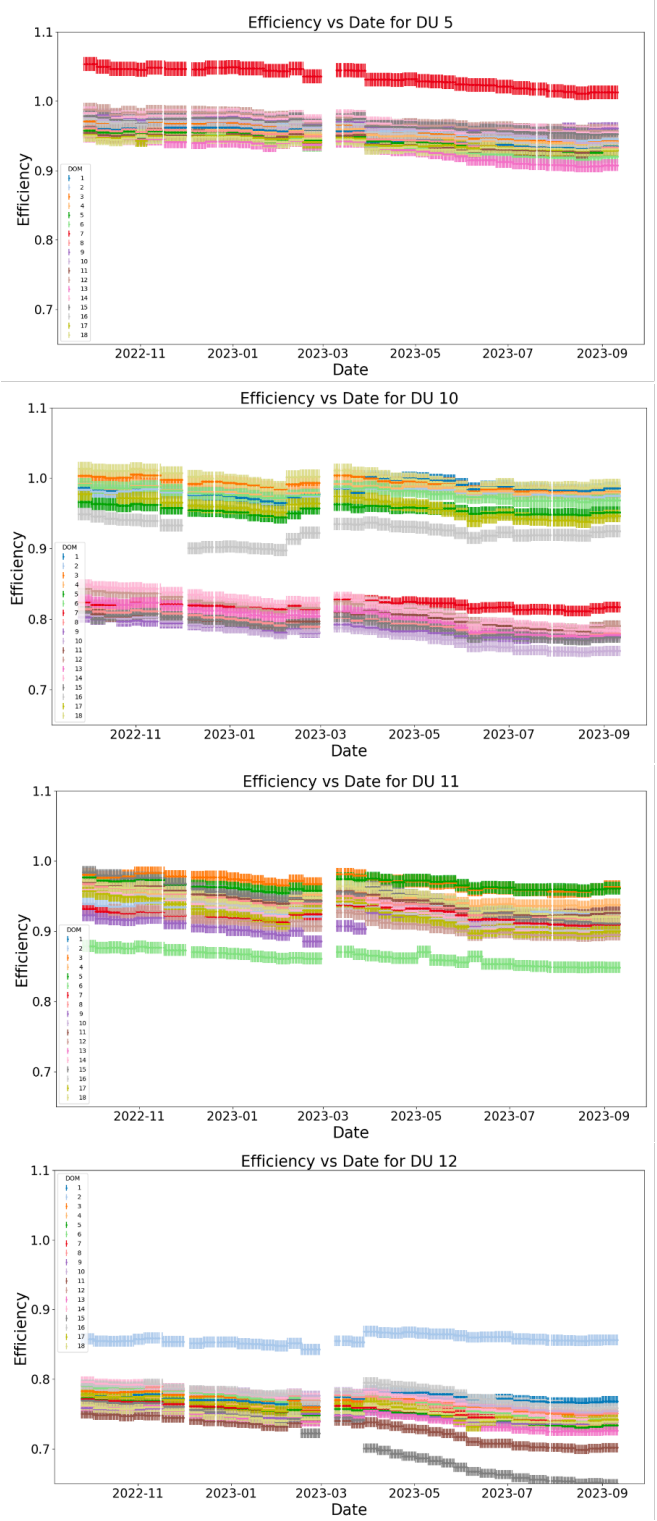

Figure 10.1: *Efficiencies of DU 5, DU 10, DU 11, and DU 12.*

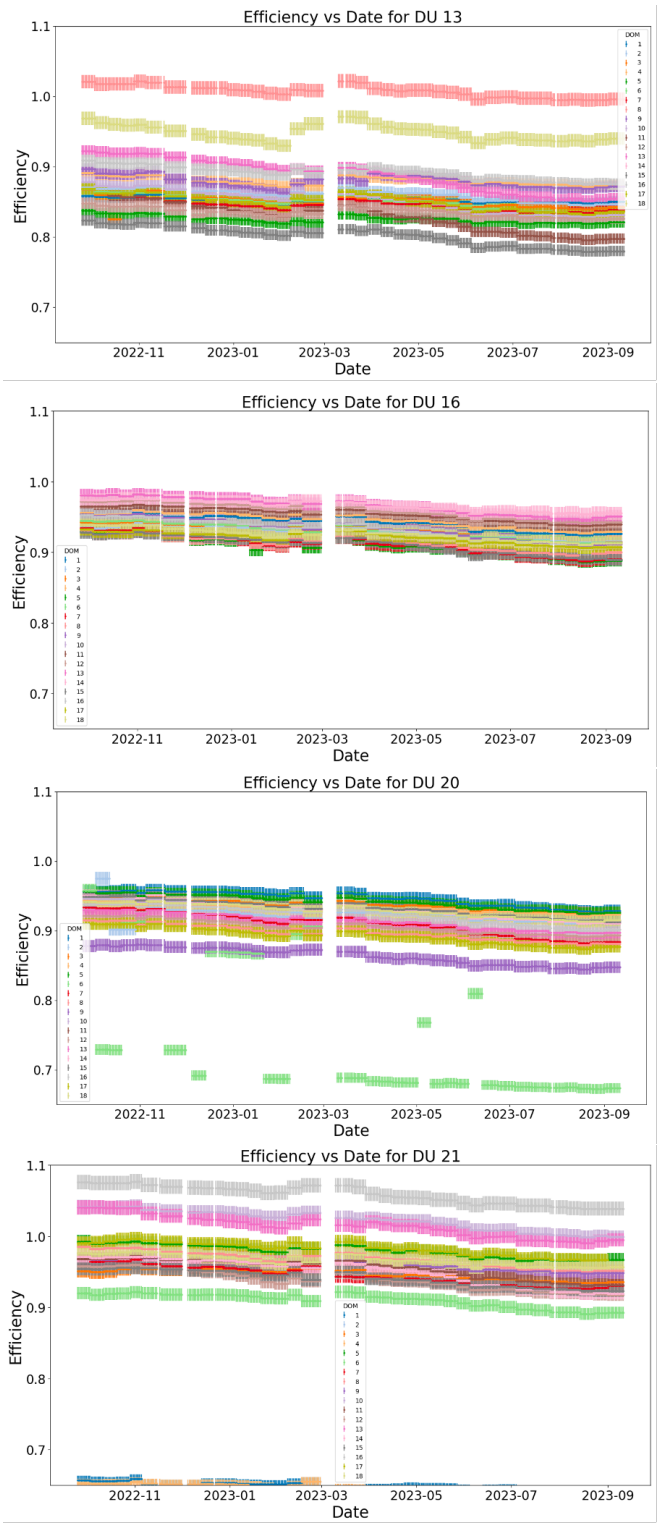

Figure 10.1: *Efficiencies of DU 13, DU 16, DU 20, and DU 21.*

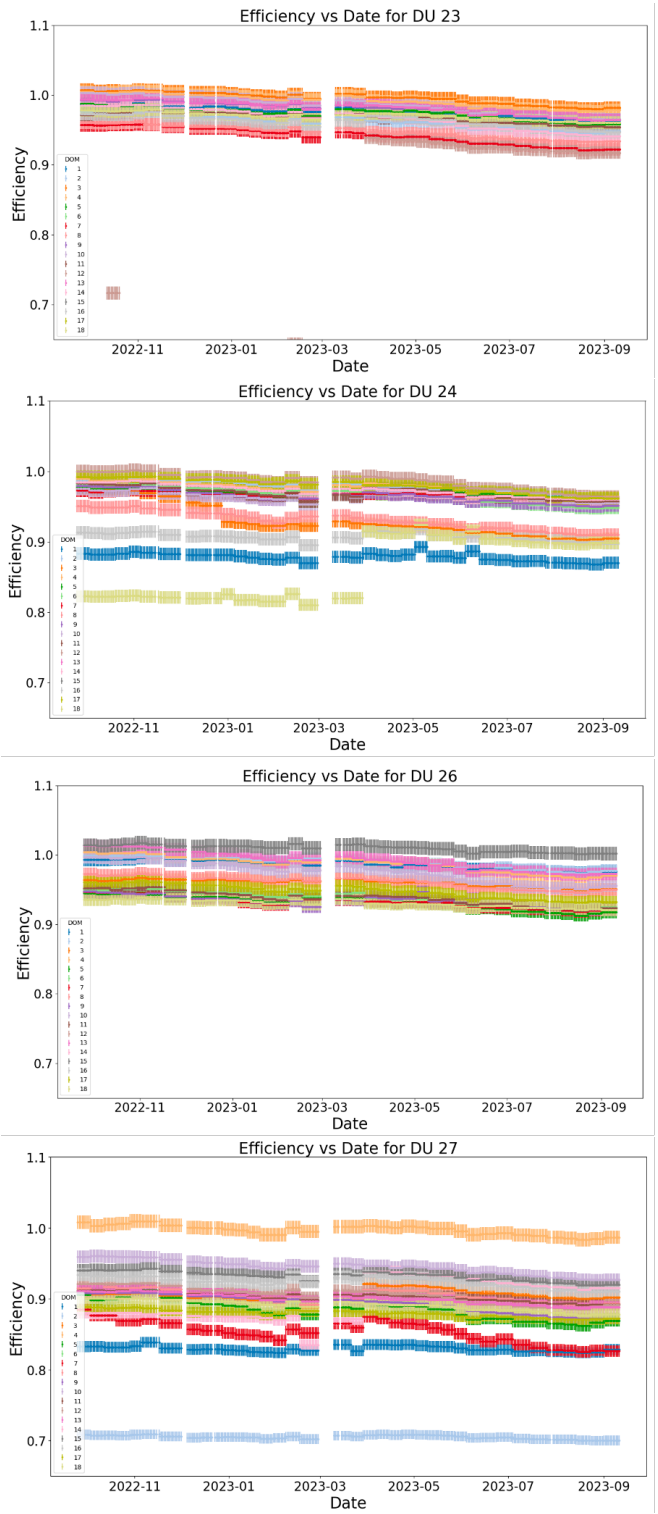

Figure 10.1: *Efficiencies of DU 23, DU 24, DU 26, and DU 27.*

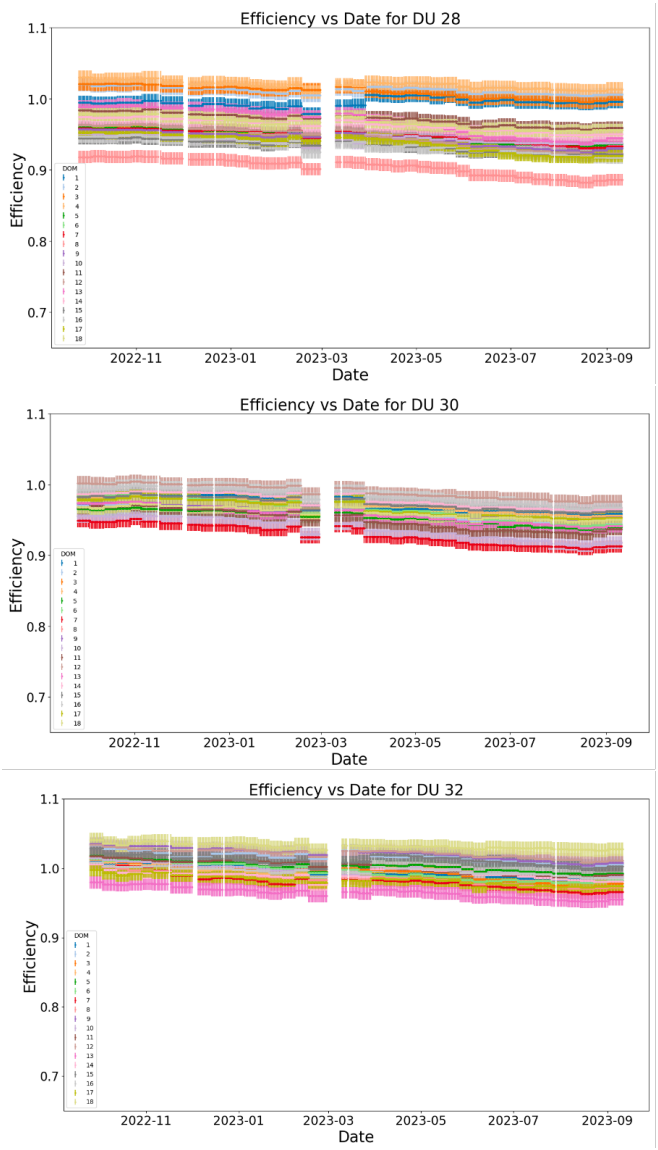

Figure 10.1: *Efficiencies of DU 28, DU 30, and DU 32.*